Competition between kinematic and dynamic waves in floods on steep slopes

P. BOHORQUEZ†

School of Architecture, Civil and Environmental Engineering, École Polytechnique Fédérale de Lausanne, 1015 Lausanne, Switzerland

We present a theoretical stability analysis of the flow after the sudden release of a fixed mass of fluid on an inclined plane formally restricted to relatively long time scales, for which the kinematic regime is valid. Shallow-water equations for steep slopes with bed stress are employed to study the threshold for the onset of roll waves. An asymptotic solution for long-wave perturbations of small amplitude is found on background flows with a Froude number value of 2. Small disturbances are stable under this condition, with a linear decay rate independent of the wavelength and with a wavelength that increases linearly with time. For larger values of the Froude number it is shown that the basic flow moves at a different scale than the perturbations, and hence the wavelength of the unstable modes is characterized as a function of the plane-parallel Froude number Fr_p and a measure of the local slope of the free-surface height ϕ by means of a multiple-scale analysis in space and time. The linear stability results obtained in the presence of small non-uniformities in the flow, $\phi > 0$, introduce substantial differences with respect to the plane-parallel flow with $\phi = 0$. In particular, we find that instabilities do not occur at Froude numbers Fr_{cr} much larger than the critical value 2 of the parallel case for some wavelength ranges. These results differ from that previously reported by Lighthill & Whitham (*Proc. R. Soc.* A, vol. 229, 1955, pp. 281–345), because of the fundamental role that the non-parallel, time-dependent characteristics of the kinematic-wave play in the behaviour of small disturbances, which was neglected in their stability analyses. The present work concludes with supporting numerical simulations of the evolution of small disturbances, within the framework of the frictional shallow-water equations, that are superimposed on a base state which is essentially a kinematic wave, complementing the asymptotic theory relevant near the onset. The numerical simulations corroborate the cutoff in wavelength for the spectrum that stabilizes the tail of the dam-break flood.

1. Introduction and motivation

This study is motivated by a wish to characterize the threshold for the onset of roll waves arising in dam-break water floods on a uniformly sloping bed for long time scales (see figure 1; Logan & Iverson 2007). Development of rollwaves about pure

† Present address: Área de Mecánica de Fluidos, Departamento de Ingeniería Mecánica y Minera, Universidad de Jaén. Campus de las Lagunillas, 23071 Jaén, Spain. Email address for correspondence: patricio.bohorquez@gmail.com

(*a*)　　　　　　　　　　　　　　　　　　(*b*)

(*c*)

FIGURE 1. Photographs of a dam-break water flood descending the US Geological Survey debris-flow flume in the H. J. Andrews Experimental Forest, Oregon (Logan & Iverson 2007): front view (*a*) of a 6 m^3 flood surge (the person in the foreground on the left-hand side provides an indication of scale), oblique view (*b*) from the right-bank platform of roll waves close to the depth sensor at a distance of 66 m from the gate and plan view (*c*) of water discharging at the end of the flume, showing many of the surface features of strong turbulence. The flume is a reinforced concrete channel 95 m long, 2 m wide and 1.2 m deep that slopes 31° (60 %).

clear-water dam-break flows is an exceptional physical phenomenon that uniquely happens when the flood wave spreads over extremely long distances: the steeper the bed slopes, the shorter the distance required. Figure 1(*a*) shows a front view of the final stage of a water dam-break flood at the US Geological Survey debris-flow flume (95 m long, 60 % slope), where hydrodynamic instabilities developed at late time. A closer view of the water surface at a distance of 66 m from the gate is

depicted in figure 1(*b*), which shows details of roll waves that are distorted because of strong turbulence. Complex structures at the free surface are better illustrated further downstream, where the Reynolds number is maximum, as shown in figure 1(*c*). Understanding how roll waves arise in dam-break flows is important because of practical implications for sediment transport. However, details of the circumstances under which roll waves occur are not understood, and such understanding forms the main aim of the current paper. As the problem is not solvable analytically, we restrict attention to a simple hydraulic model that illustrates the basic ideas. The theoretical analysis will be based on the one-dimensional shallow-water equations for steep slopes with bed stress.

The influence of bed slope for large Reynolds numbers is of great interest for the obvious reason that catastrophic flooding associated with the sudden drainage of glacier- or moraine-impounded lakes as well as the break of man-made concrete dams occurs over topographies that are not horizontal (e.g. Bohorquez & Darby 2008; Denlinger & O'Connell 2008). The bed slope effect, in the dam-break problem of a finite mass of fluid on an inclined plane, was analysed by Dressler (1958) without considering bed stress. After establishing that one can determine analytically the exact wavefront celerity (neglecting resistance) for the case where the bottom is inclined below the horizontal' (Dressler 1952, p. 217), he presented in 1958 an exact solution for ideal (frictionless) dam-break floods on an inclined plane 'for slopes which are not excessive'. Later, Hunt (1987) presented a similar solution. Since the earlier work of Dressler other solutions valid for steep slopes have been obtained (Fernandez-Feria 2006; Ancey *et al.* 2008). However, similar to the horizontal problem (e.g. Schoklistsch 1917; Eguiazaroff 1935; Dressler 1952; Martin & Moyce 1952; Dressler 1954; Whitham 1955; Lauber & Hager 1998*a*; Hogg & Pritchard 2004; Jánosi *et al.* 2004), hydraulic resistance cannot be neglected in floods over inclined planes (e.g. Lauber & Hager 1998*b*). This fact was originally noted by Lighthill & Whitham (1955), who established that flood waves on inclined planes can be described as kinematic waves (i.e. waves in which a balance is struck between frictional and gravitational forces) for subcritical floods. In this case, hydraulic resistance affects not only the advancing of the forward wave but also the bulk of the flow when the flood travels approximately four times its initial extent (Hunt 1982). Moreover, kinematic waves and dynamic waves are both possible together in supercritical floods (Lighthill & Whitham 1955). In supercritical streams, kinematic and dynamic waves can play equally important parts, as in the case of 'roll waves' observed in mountain streams (e.g. Dressler 1954). This behaviour is essentially different from that of an ideal (frictionless) wave, which constitutes a purely dynamic wave. Therefore, the importance of considering frictional effects in floods on inclines (e.g. Lauber & Hager 1998*b*) questions the applicability of ideal solutions to real scenarios. The hydraulic effect in a dam-break flood over an incline of shallow slope was studied analytically by Hunt (1982) and later in floods of a point source of mass by Weir (1983) and Hunt (1984). Weir and Hunt claimed that the resulting flow at late time does not depend on its initial configuration. This was corroborated by comparison of theoretical solutions with laboratory data.

As commented above, a thin layer of water flowing down an inclined surface may undergo, in some circumstances, a transition to an oscillatory movement, where a train of surface waves propagates downstream. The development of roll waves happens for large Reynolds numbers, typically above 400 for quasi-two-dimensional roll waves and above 1200 for roll waves for turbulent flow. In this region of fairly large Reynolds numbers the velocity can be assumed to be independent of the cross-stream

coordinate, leading to the shallow-water or Saint-Venant equations (Saint-Venant 1871; Whitham 1974). The evolution of the surface is governed by a sequence of transitions starting from the primary instability of the plane-parallel flow, filtering mechanism of the linear instability and secondary modulation instability that converts the primary wave field into a roll wave (e.g. Prokopiou, Cheng & Chang 1991; Ruyer-Quil 2006). These hydrodynamic instabilities have been observed in laboratory flumes (Brock 1969; Brauner & Maron 1982). Two main approaches can be followed to establish the stability criteria of the plane-parallel flow: first, the hydraulic one, which finds long travelling-wave solutions for Froude numbers above 2 by means of the shallow-water equations (e.g. Jeffreys 1925; Dressler 1949; Needham & Merkin 1984; Hwang & Chang 1987; Yu & Kevorkian 1992; Chang, Demekhin & Kalaidin 2000); second, on the basis of the linearized Reynolds equations for a turbulent flow, with critical Froude numbers varying between 1.1 and 1.4 as the Reynolds number is varied over the realistic range of values 2×10^3–10^5 (Demekhin, Kalaĭdin & Shapar' 2005). The effect of bottom topography on the stability of a turbulent flow over uneven surfaces was recently explored by Balmforth & Mandre (2004) following the hydraulic approach, who found that low-amplitude topography destabilizes turbulent roll waves and lowers the critical value of the Froude number required for instability. In a general case concerning curved solid walls, roll waves are possible, and the slope of the wave profile is no longer constant but varies slowly in the streamwise direction (Kluwick 2006). Roll waves are also observed in clear-water dam-break floods over man-made channels of uniform, steep slope (Logan & Iverson 2007). In the experiments conducted on 30 August 1994, 28 August 2002 and 7 June 2006 at the US Geological Survey debris-flow flume, it was found that instabilities develop at late time when the bulk of the flood wave reaches a quasi-uniform and quasi-steady state. Roll waves in floods on inclines were also found by Bohorquez & Fernandez-Feria (2008) in the numerical computations of sediment transport associated with this flow, which were not taken into account in the analytical predictions by Pritchard (2005). This behaviour, termed 'competition between kinematic and dynamic waves', is that which was figured out by Lighthill & Whitham (1955) more than half a century ago. The flow changes from a quasi-uniform and quasi-steady state to a highly unsteady one.

Apart from their interest in hydraulic and environmental engineering, in which turbulent roll waves enhance the transport of sediment and the risk of infrastructure damage, the development of hydrodynamic instabilities in kinematic waves constitutes a non-modal stability problem of great interest, in which the non-parallel time-varying characteristics of the base flow may affect significantly the stability criterion for the onset of roll waves and the wavelength behaviour of small disturbances (Schmid 2007). Therefore, this paper is aimed at reviewing and extending the linear stability criteria in combination with validating numerical simulations for the inception of roll waves in floods on uniform slopes in the kinematic regime – the study of the dynamics of roll waves about kinematic waves is outside the scope of the current work. We start with the formulation of the problem and the definition of the basic flow (§2). Next in §3.1, the particular case with a Froude number of 2, which represents the stability criterion for the parallel case, is analysed. Subsequently, we perform a linear stability analysis by means of multiple scales for Froude numbers larger than 2 and draw out the connections between this analysis and the previous one by Lighthill & Whitham (§3.2). The main new features are that non-parallel time-varying effects originating from the slow streamwise variations of the background

flow are taken into account. Then, we present some numerical simulations for the perturbations based on the shallow-water equations (§ 3.3) and compare the numerical growth rate with the asymptotic predictions, showing the applicability of our theoretical findings. The link between the asymptotic analysis and the case with actual release of a fixed mass of fluid is made in § 3.4. Finally, we draw some conclusions.

2. Formulation of the problem

In the shallow-water approximation, the dimensionless equations for the mass conservation and momentum in the direction of the flow over a constant slope bed can be written as (Dressler 1978)

$$\frac{\partial \eta}{\partial t} + \frac{\partial \eta U}{\partial X} = 0, \tag{2.1}$$

$$\frac{\partial U}{\partial t} + U \frac{\partial U}{\partial X} + \cos\theta \frac{\partial \eta}{\partial X} = \sin\theta - \frac{s_f}{\eta}, \tag{2.2}$$

where θ is the angle between the bed and the horizontal; t is time; X is the coordinate along the bed; η is the depth of the water measured along the coordinate Y perpendicular to the bed; U is the depth-averaged velocity component along X; and s_f is a dimensionless bed friction (see below). All the variables in these equations have been non-dimensionalized with respect to a length scale η_0, corresponding to some initial depth, and a velocity scale $U_0 \equiv \sqrt{g\eta_0}$, where g is the acceleration because of gravity. To compute the friction term $s_f \equiv (\tau_b/\rho U_0^2)$, where τ_b is the scaled bed stress and ρ the fluid density, we shall use the Darcy–Weisbach friction factor f, so that s_f may be written as

$$s_f = \frac{f}{8} |U|U. \tag{2.3}$$

The factor f is a function of the local Reynolds number, based on the velocity U and the hydraulic radius of the channel, and of the relative height roughness of the bed. We shall assume that the friction factor f is constant to make the analytical treatment feasible.

The initial conditions for the flood wave that results after the rupture of a dam on an incline may be idealized as a point source of mass initially at rest located at $X = 0$ (Weir 1983; Hunt 1984):

$$U(X, 0) = 0, \quad \eta(X, 0) = A\delta(X), \quad 0 < X, \tag{2.4}$$

where A is the non-dimensional released volume of water per unit width and $\delta(X)$ is the Dirac delta function.

Whilst the non-dimensional variables X and t are appropriate to describing the evolution of dynamic waves, as in the absence of hydraulic resistance, kinematic waves vary on a much slower scale:

$$\hat{x} = \epsilon X, \quad \hat{t} = \epsilon t \quad \text{with} \quad \epsilon \equiv \frac{\eta_0}{l} \ll \sin\theta \quad \text{and} \quad 0 < \theta < \pi/2, \tag{2.5}$$

where l is the characteristic streamwise extent occupied by the flood wave and ϵ is the shallowness parameter. In these new variables, (2.1)–(2.3) read

$$\frac{\partial \eta}{\partial \hat{t}} + \frac{\partial \eta U}{\partial \hat{x}} = 0, \tag{2.6}$$

$$\epsilon \left(\frac{\partial U}{\partial \hat{t}} + U \frac{\partial U}{\partial \hat{x}} + \cos\theta \frac{\partial \eta}{\partial \hat{x}} \right) = \sin\theta - \frac{f U^2}{8\eta}, \tag{2.7}$$

allowing the solution of the flood wave (i.e. the basic flow, hereafter denoted by the subscript b) to be written in powers of ϵ:

$$\eta_b(\hat{x}, \hat{t}) = H_0(\hat{x}, \hat{t}) + \epsilon H_1(\hat{x}, \hat{t}) + O(\epsilon^2), \tag{2.8}$$
$$U_b(\hat{x}, \hat{t}) = V_0(\hat{x}, \hat{t}) + \epsilon V_1(\hat{x}, \hat{t}) + O(\epsilon^2). \tag{2.9}$$

Substituting expansion (2.8)–(2.9) into (2.7), and grouping terms of order unity, one obtains the algebraical relation that follows between H_0 and V_0:

$$H_0 = \frac{f V_0^2}{8 \sin\theta}. \tag{2.10}$$

Analogously, taking into account (2.10), order unity of (2.6) provides the well-known kinematic-wave equation

$$\frac{\partial V_0}{\partial \hat{t}} + \frac{3 V_0}{2} \frac{\partial V_0}{\partial \hat{x}} = 0, \tag{2.11}$$

showing that H_0 and V_0 remain constant for characteristics propagating with velocity $(3/2)V_0$. Substituting (2.10) into (2.7) and using (2.11), one obtains the following condition for the validity of this approximation:

$$\epsilon \left| \frac{\partial H_0}{\partial \hat{x}} \right| \ll \left| \frac{\sin\theta}{\cos\theta - \frac{2}{f}\sin\theta} \right|. \tag{2.12}$$

Equation (2.11) is exactly the same as that considered by Lighthill & Whitham (1955) on the prediction of flood movement in man-made channels. Later on, Weir (1983) and Hunt (1984) provided the solution of this equation, together with the initial conditions given by (2.4) but starting their analyses from the traditional Saint-Venant equations. Since their studies idealize the initial volume of water at rest as a point mass source initially located at the origin $\hat{x} = 0$ (see the initial condition (2.4)), both solutions can certainly be reformulated to steep slopes by rewriting them in the appropriate set of non-dimensional variables (Dressler 1978). On the one hand, Weir (1983) and Hunt (1984) provided the so-called leading-order outer solution of the dam-break wave, that is the solution to (2.11) for the initial condition (2.4),

$$U(\hat{x}, 0) = 0, \quad \eta(\hat{x}, 0) = A^* \delta(\hat{x}), \quad A^* \equiv \epsilon A, \quad 0 < \hat{x}. \tag{2.13}$$

Conservation of mass is imposed by means of a shock $\hat{x}_s(\hat{t})$ inserted in the dam-break wavefront, i.e.

$$\int_0^{\hat{x}_s(\hat{t})} H_0(\hat{x}, \hat{t}) \, d\hat{x} = A^*. \tag{2.14}$$

To be consistent with volume conservation (see Ancey, Cochard & Andreini 2009), we select the aspect-ratio number ϵ as $A^* = \epsilon A = 1$, that is

$$\epsilon = \frac{1}{A} = \frac{\eta_0^2}{\widetilde{A}}, \tag{2.15}$$

in which $\tilde{A}$ is the dimensional volume of fluid per unit width released at $\hat{t} = 0$. The value of the characteristic water depth η_0 is discussed below. Hence, the outer solution is given by

$$V_0(\hat{x}, \hat{t}) = \frac{2\hat{x}}{3\hat{t}} \quad \text{for} \quad 0 \leqslant \hat{x} \leqslant \hat{x}_s(\hat{t}) \equiv \left(\frac{54 \sin \theta}{f} \hat{t}^2 \right)^{1/3}, \quad 0 < \hat{t}. \quad (2.16)$$

On the other hand, Hunt (1984) improved Weir's study matching the outer solution with that within the tip region of the dam-break flood, referred to as 'inner' solution, whose relative length remains small as the current lengthens (see the original work by Hunt 1984 for further details).

Higher-order terms of the outer expansion (2.8)–(2.9) can be integrated recursively along the family of characteristic curves $\hat{x}/\hat{t} = \text{constant}$ (see Appendix A), with V_j and H_j $(1 \leqslant j)$ vanishing as $\hat{t} \to \infty$, whilst V_0 and H_0 remain constant. Furthermore, the leading-order terms in (2.8) and (2.9) that satisfy the kinematic-wave equations (2.10) and (2.11) are exact solutions to the full shallow-water equations (2.6) and (2.7) when $f = 2 \tan \theta$. This is due to the fact that the left-hand side of (2.7) vanishes. Conversely, for $f \neq 2 \tan \theta$, the left-hand side of (2.7) introduces higher-order corrections in expansion (2.8)–(2.9), and the characteristic time necessary to neglect higher-order-terms can be estimated by means of (2.12) at the shock $\hat{x}_s(\hat{t})$. Indeed, the non-dimensional characteristic time $\hat{t}_c$ is defined as function of a tolerance Φ which describes how well (2.12) is satisfied: it is obtained by setting the left-hand side of (2.12) equal to the product of Φ and the right-hand side of (2.12), substituting in the kinematic-wave solution (2.10)–(2.16), evaluating it at the front of the wave $\hat{x}_s(\hat{t})$ and solving for $\hat{t}$,

$$\hat{t}_c < \hat{t} \quad \text{with} \quad \hat{t}_c \equiv \left(\frac{\epsilon}{\Phi} \right)^{3/4} \sqrt{\frac{1}{\sin \theta}} \left(\frac{2|f - 2\tan\theta|^3}{27 f (\tan \theta)^3} \right)^{1/4}. \quad (2.17)$$

Evaluating the outer solution (2.10)–(2.16) at $\hat{x}_s(\hat{t}_c)$, taking into account the definition of ϵ, given by (2.15) and posing $H_0(\hat{x}_s(\hat{t}_c), \hat{t}_c) = 1$ yields the dimensional characteristic water depth:

$$\eta_0 = \left(\frac{3\tilde{A} \, \Phi \, f \tan \theta}{2|f - 2\tan\theta|} \right)^{1/2}. \quad (2.18)$$

The local Froude number of the base state $[\eta_b(\hat{x}, \hat{t}), U_b(\hat{x}, \hat{t})]^T$ (the superscript T denotes transposed vector) is defined by

$$Fr \equiv \frac{U_b}{\sqrt{\eta_b \cos \theta}} = \frac{V_0}{\sqrt{H_0 \cos \theta}} + \epsilon \frac{\cos \theta (2 H_0 V_1 - H_1 V_0)}{2(H_0 \cos \theta)^{3/2}} + O(\epsilon^2). \quad (2.19)$$

Under condition (2.17), it tends to the constant value of the plane-parallel flow, denoted hereafter by Fr_p. In fact, substituting (2.10) into (2.19), we find

$$Fr = Fr_p + O(\epsilon) \approx Fr_p \quad \text{with} \quad Fr_p \equiv \frac{V_0}{\sqrt{H_0 \cos \theta}} = \sqrt{\frac{8}{f} \tan \theta} \quad \text{for} \quad \hat{t}_c < \hat{t}. \quad (2.20)$$

Finally, we make a definition for the measure of the local slope of the free-surface height (ϕ) that is employed in the multiple-scale stability analysis (see §3.2),

$$\phi \equiv \epsilon \frac{4}{f} \frac{\partial H_0}{\partial \hat{x}} = \epsilon \frac{V_0}{\sin \theta} \frac{\partial V_0}{\partial \hat{x}}. \quad (2.21)$$

Therefore, using the definition of Fr_p, given by (2.20), and the local free-surface slope of the base state (2.21), the local-validity condition (2.12) for the kinematic-wave

approximation reads

$$|\phi| \ll \phi^* \equiv \left| \frac{2}{4\varrho - 1} \right| \quad \text{with} \quad \varrho \equiv \frac{1}{Fr_p^2}. \tag{2.22}$$

Notice that ϕ^* decreases from ∞ to the limiting value of 2 as Fr_p varies in the range of values $[2, \infty)$.

As problems of physical significance are rather involved and not solvable analytically, for instance because of non-uniform time-varying friction factors, we restrict attention to the present simple model that illustrates the basic ideas: for instance, we shall see below that roll waves develop in the bulk of the near-equilibrium dam-break wave, far from the tip region, when the friction factor f takes a constant value, about a background flow that is essentially a kinematic wave; and thus, in the next section (§3), we perform the linear stability analysis of the outer solution (2.16).

In order to check the correctness of the kinematic-wave approximation for predicting flood waves, the initial configuration for a dam-break flow on an inclined plane sketched in figure 2(a):

$$U(X, 0) = 0, \quad \eta(X, 0) = \begin{cases} 0 & \text{for } X < -\Upsilon/e, \\ eX + \Upsilon & \text{for } -\Upsilon/e \leqslant X \leqslant 0, \\ -X/e + \Upsilon & \text{for } 0 < X \leqslant e\Upsilon, \\ 0 & \text{for } X > e\Upsilon, \end{cases} \tag{2.23}$$

$$e \equiv \tan\theta, \quad \Upsilon \equiv \sqrt{\frac{e\tilde{A}}{(1 + e^2)\eta_0^2}},$$

is considered as the benchmark case and is solved with the numerical technique detailed in Bohorquez & Fernandez-Feria (2008). Without losing generality, we have chosen $\Phi = 0.3769$ to make the variables dimensionless. Figure 2(b) shows the velocity profiles at the inception of roll waves ($t > 4408$) for a volume of water per unit width $\tilde{A} = 57.31 \text{ m}^2$, a plane inclined at an angle of $1°$ with respect to the horizontal and a flow with plane-parallel Froude number $Fr_p = 2.5$. In doing so, the ensuing friction factor takes a plausible physical value ($f = 0.0223$), and the present numerical experiment can be reproduced in (laboratory) reality: for instance, instead of releasing a finite volume of water (which requires a extremely long channel), one can first create a uniform stream, attaining the desired Froude number by controlling the flume roughness, flow discharge and water depth at the flow inlet, closing progressively the inlet gate and reducing both the flow discharge and the water depth with the temporal law fixed by the kinematic-wave solution (2.10)–(2.16). This last experiment would require a shorter (cheaper) channel of shallow slope – notice that steep slope flumes are rather involved and thus scarce, and we hope that this work motivates new experiments on turbulent roll waves about kinematic waves. Moreover, as we shall see in the next sections, the most noticeable results are observed for Froude numbers slightly larger than 2.

A general view of the velocity profiles at several instants after the rupture of the dam is shown in figure 2(c). As time proceeds, the agreement between the numerical (continuous line) and the outer solution (stars), given by (2.16), continues to become better. In addition, the asymptotic solution that accounts for the initial profile of the water height (2.23) is also shown in the same figure (circles). The latter solution, which was provided originally by Hunt (1982) for small bottom slopes, cannot be reformulated to arbitrary (constant) slopes of the bottom with a simple change of variables but is to be obtained for our specific initial conditions (see Bohorquez
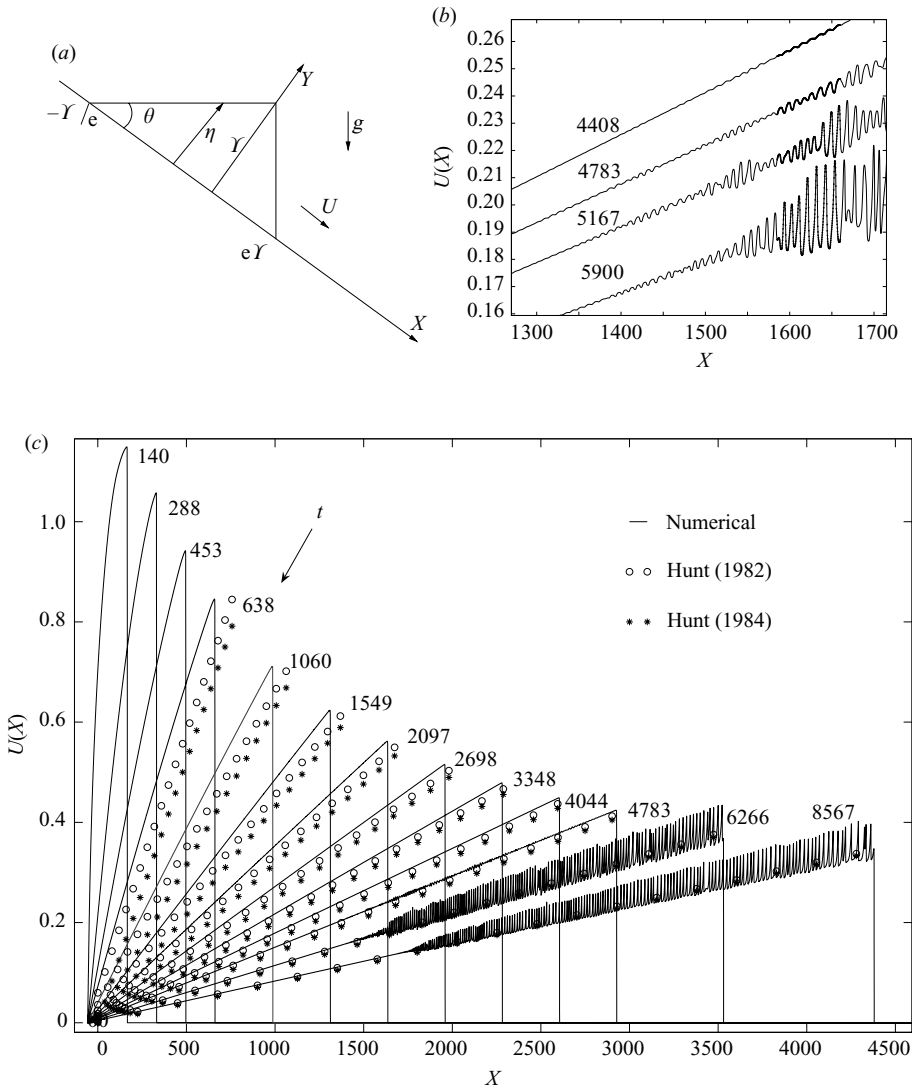
FIGURE 2. (*a*) Coordinates and sketch of the initial conditions for $\eta(X)$ in the dam-break problem on an inclined plane, given by (2.23); (*b*) onset of roll waves at $t \approx 4408$; and (*c*) velocity profiles at several instants of time for $\tilde{A} = 57.31\,\text{m}^2$, $\Phi = 0.3769$, $\theta = 1°$ and $f = 0.0223$ ($Fr_p = 2.5$). The numerical solution is plotted in the continuous line and in the circles and the stars the velocity profile corresponding to the outer solution given by Hunt (1982, 1984), generalized to steep slopes, and given by (2.16) and Bohorquez (2008, pp. 356–357), respectively. The computations were conducted with a uniform mesh size, $\Delta X = 0.2$ and a Courant-Friedrichs-Lewy member of $CFL = 0.45$. The dots in (*b*) show the computational nodes within the range $1585 < X < 1660$, indicating that jiggles are well resolved.

2008, pp. 356–357). It is corroborated that the flow forgets its initial configuration at late time (i.e. $t \approx 4044$), when the two asymptotic solutions and the numerical one are almost indistinguishable. Subsequently, reliable estimates of Φ in (2.17) can be derived from the characteristic time for the present scenario: substituting the values $\{\Phi = 0.3769,\ \tilde{A} = 57.31\ \text{m}^2,\ f = 0.0223,\ \theta = 1°\}$ into (2.15), (2.17) and (2.18), and taking into account (2.5), yields $t_c \approx 45.81$; however, as shown in figure 2(*c*), we

have to wait until $t \gg 45$ for the deviation between the numerical and asymptotic solution (2.16) to drop to zero; in order to establish a criteria for the election of Φ, we impose that the relative deviation between the slope of the asymptotic and numerical velocity profiles at t_c should be lower than 4.5%; in the present numerical simulation this deviation occurs at $t_c \approx 4000$, and by setting $\Phi \approx 4.25 \times 10^{-3}$ (instead of $\Phi = 0.3769$) one obtains approximately such value of t_c. So it is found that the numerical solution converges rather slowly towards the outer solution (as for the dam-break flow for viscous fluids in the high-capillary-number limit for non-zero bed slopes; see Ancey *et al.* 2009). However, the main feature of real flood waves on steep inclines in relation to the predictions of the asymptotic solutions is the appearance of roll waves. For long times, the balance between friction and gravity in the bulk of the flood wave is more and more exact. The more exact friction–gravity balance makes instabilities more likely, as in the case of a uniform stream with $Fr_p > 2$. So we observe the formation of instability at the free surface. The onset of these roll waves is located in the bulk of the flow, far from the tip region, and their amplitudes grow, ultimately developing hydraulic jumps, which are convected towards the wetting front. The possible sources of numerical error that induce the appearance of roll waves are various, namely the convergence error measure (Castro, Gallardo & Parés 2008), the stiffness of the hyperbolic balance laws (2.1) and (2.2) with non-trivial moving-water solution determined by the asymptotic balance of the source term for long time scales (e.g. Dumbser, Enaux & Toro 2008), the critical point ($Fr = 1$) moving from $X = 0$ at $t = 0$ towards the drying front ($X = -\Upsilon/e$ at $t \to \infty$) (we notice that although the entropy correction for transonic rarefactions attenuates numerical discontinuities at critical points, they never vanish) and the forcing of the round-off numerical noise.

Lighthill & Whitham (1955) established the stability criterion for kinematic waves by means of a linear stability analysis of the nonlinear shallow-water equations and also by introducing discontinuities in the first derivatives of U and η as typical disturbances. Their results are based on the plane-parallel Froude number Fr_p, which equals the Froude number Fr when an exact balance is struck between the bottom friction and the streamwise component of gravity. As discussed above, this particular case is only possible for kinematic waves when $Fr_p = 2$, for which $H_j = V_j = 0$ for $j \geqslant 1$, or as $\hat{t} \to \infty$ when $Fr_p \neq 2$. Their linear stability analysis does not account for non-parallel time-dependent effects originating from slow streamwise variations of the base flow on the stability criterion (see Lighthill & Whitham 1955, p. 292, simplification (iv): 'In the undisturbed flow, we suppose that η_b and U_b take constant values ... ') and establishes that background flows with $Fr_p = 2$ are unstable (see Lighthill & Whitham 1955, equation (23)). This result differs from that for turbulent uniform flow on an inclined plane, which is critically stable for $Fr_p = 2$ but unstable at all wavenumbers when the Froude number is greater than 2 (Jeffreys 1925).

The next section is devoted to exploring non-parallel time-varying effects (originating from the slow streamwise variations of the background flow) on linear, local stability results of the kinematic base state (2.16) for long time scales (i.e. $\hat{t} \geqslant \hat{t}_c$). To that end, the kinematic-wave solution (2.10)–(2.16) is rewritten as

$$V_0(\hat{x}, \hat{t}^*) = \frac{\hat{\vartheta}\hat{x}}{1 + \frac{3}{2}\hat{\vartheta}\hat{t}^*}, \quad H_0 = \frac{fV_0^2}{8\sin\theta}, \quad 0 \leqslant \hat{x} \leqslant \hat{x}_s(\hat{t}^* + \hat{t}_c), \quad 0 \leqslant \hat{t}^*, \qquad (2.24)$$

in which $\hat{\vartheta}$ is the slope of the velocity profile at time $\hat{t} = \hat{t}_c$,

$$\hat{\vartheta} \equiv \frac{2}{3\hat{t}_c}, \qquad (2.25)$$

and the temporal coordinate is redefined as $\hat{t}^* \equiv \hat{t} - \hat{t}_c$. In doing so, the influence of the streamwise variation of the background-flow velocity profile $\hat{\vartheta}$ is included in the results of the stability analysis, and it will ease the comparison of the asymptotic results (§§ 3.1 and 3.2) with the nonlinear numerical simulation of the disturbance evolution (§ 3.3) with initial conditions (3.45). The main drawback of this approach is that the influence of higher-order corrections of the base flow are neglected in the stability analysis, restricting the applicability of the stability results to long times, $\hat{t} \gg \hat{t}_c$. In addition, for the physical reasons previously discussed, the numerical results in § 3.3 correspond to shallow slopes of the bottom bed, although the asymptotic study presented in §§ 3.1 and 3.2 is valid for steep slopes. Finally, in the analyses that follow (for notational clarity) the asterisk notation is dropped, and the stability results henceforth correspond to those of a dam-break flow at long times.

3. Results

3.1. *Asymptotic solution for $Fr_p = 2$*

As stated in § 2, the leading-order terms in expansion (2.8)–(2.9) that satisfy the kinematic-wave equations (2.10) and (2.11) are exact solutions to the full shallow-water equations (2.6) and (2.7) when $Fr_p = 2$, because the left-hand side of (2.7) vanishes. In order to analyse the stability of the background flow (2.24) with $Fr_p = 2$ and capture the non-modal behaviour of small disturbances, avoiding the misrepresentation of the disturbance transient behaviour, we express the basic flow (2.24) in the rapid scale variables X and t,

$$U_b(X,t) = \frac{2}{3} B \, \xi(X,t), \quad \eta_b = \frac{f U_b^2}{8 \sin\theta}, \quad B \equiv \frac{3}{2}\vartheta, \quad \vartheta \equiv \epsilon\hat{\vartheta},$$
$$0 \leqslant X \leqslant X_s(t + t_c), \quad 0 \leqslant t. \tag{3.1}$$

In the equation shown above, we have introduced a new variable, namely

$$\xi(X,t) \equiv \frac{X}{1 + Bt}, \tag{3.2}$$

and to simplify the notation, it is also convenient to redefine the temporal coordinate as

$$\tau(t) \equiv 1 + B\,t. \tag{3.3}$$

Notice that (3.1)–(3.3) are an exact solution to the shallow-water equations (2.1)–(2.3) for $Fr_p = 2$ at all positive value of $\hat{\vartheta}$ (2.25). Dimensionally or in relation to the kinematic-wave approximation, this means that $\hat{t}_c$ is not required to be large.

Now, the perturbed flow is decomposed, as usual, as the sum of the basic flow solution, η_b and U_b, plus a small perturbation, $h(X,t)$ and $u(X,t)$,

$$\eta = \eta_b + h, \quad U = U_b + u, \tag{3.4}$$

with the initial conditions

$$h(X,0) = \sum_{j=1} \upsilon^j \, p_j(X), \quad u(X,0) = \sum_{j=1} \upsilon^j \, q_j(X), \quad 0 \leqslant X \leqslant X_s(t_c), \tag{3.5}$$

in which υ is a positive small parameter that measures the relative amplitude of the initial disturbance. The shape of the initial condition $[p_j(X), q_j(X)]^T$ compatible with solutions to the system of partial differential equations governing the evolution of small disturbances is discussed below.

To find out the asymptotic solution to the linear and nonlinear evolution of small disturbances, the (non-dimensional) perturbation $\mathbf{s} \equiv [h(X, t), u(X, t)]^T$ is expanded in the form

$$\mathbf{s}(X, t) = \sum_{j=1} \upsilon^j \, \mathbf{s}_j. \tag{3.6}$$

The first term in the expansion must satisfy

$$\upsilon \, ||\mathbf{s}_1|| \ll ||(\eta_b, U_b)^T||, \tag{3.7}$$

whilst the subsequent terms must satisfy $\upsilon \, ||\mathbf{s}_j|| \ll ||\mathbf{s}_{j-1}|| \, (1 < j)$. We shall also assume that the streamwise variation of the basic flow is small,

$$\left| \frac{\partial \eta_b}{\partial X} \right| \ll 1, \quad \left| \frac{\partial U_b}{\partial X} \right| \ll 1. \tag{3.8}$$

Substituting (3.4) into (2.1)–(2.3), taking into account that $[\eta_b, U_b]^T$ is a solution to the equations and that $Fr_p = 2$ and neglecting the second-order terms in both the small perturbations and the streamwise derivatives of the basic flow, one is left with the following set of linear equations for the perturbations:

$$\frac{\partial \mathbf{s}_1}{\partial t} + \mathbf{A} \cdot \frac{\partial \mathbf{s}_1}{\partial X} + (\mathbf{B} + \mathbf{C}) \cdot \mathbf{s}_1 = 0, \quad 0 \leqslant X \leqslant X_s(t + t_c), \quad 0 \leqslant t, \tag{3.9}$$

with homogeneous upstream (supercritical) boundary conditions (BCs)

$$\mathbf{s}_1(0, t) = 0, \quad 0 < t, \tag{3.10}$$

where

$$\mathbf{A} \equiv \begin{pmatrix} U_b & \dfrac{f U_b^2}{8 \sin \theta} \\ \cos \theta & U_b \end{pmatrix}, \quad \mathbf{B} \equiv \begin{pmatrix} 0 & 0 \\ -\dfrac{8(\sin \theta)^2}{f U_b^2} & \dfrac{2 \sin \theta}{U_b} \end{pmatrix}, \quad \mathbf{C} \equiv \begin{pmatrix} \dfrac{\partial U_b}{\partial X} & \dfrac{f U_b}{4 \sin \theta} \dfrac{\partial U_b}{\partial X} \\ 0 & \dfrac{\partial U_b}{\partial X} \end{pmatrix}. \tag{3.11}$$

Matrices $\mathbf{A}$–$\mathbf{C}$ are functions of X and t, and therefore the linear perturbation $\mathbf{s}_1$ does not admit a decomposition in normal modes. Instead, we seek solutions of the form $\mathbf{s}_1 = M_1(\tau)[h_1(\xi), u_1(\xi)]^T$. The general solution to (3.9) reads

$$\mathbf{s}_1 = \frac{F(\xi)}{\tau} \begin{pmatrix} \dfrac{f U_b(\xi)}{4 \sin \theta} \\ 1 \end{pmatrix}, \quad F(0) = 0, \tag{3.12}$$

which allows us to set a disturbance with arbitrary shape as the initial condition, $F(\xi)$. No approximation regarding the disturbance shape has been introduced so far. However, it should be pointed out that the eigenvector in (3.12) imposes a specific relation between the amplitude of the perturbation velocity and height, whose physical meaning is readily figured out: curiously, the perturbed flow also satisfies the kinematic-wave approximation,

$$h_1 = \frac{1}{M_1} \left[\frac{f}{8 \sin \theta} (U_b + M_1 u_1)^2 - \eta_b \right] \approx \frac{f}{4} \frac{U_b}{\sin \theta} u_1.$$

Hence, the base flow contains stable small disturbances, and their dynamics is given by the regular expansion (2.8)–(2.9), propagating and attenuating with the kinematic wave

itself. Indeed, small disturbances (3.12) are attenuated as the first-order corrections of the base flow ((A 5) and (A 7)).

In general, one can find nonlinear corrections to this solution as

$$\mathbf{s}_j \equiv M_j(\tau) \begin{pmatrix} h_j(\xi) \\ u_j(\xi) \end{pmatrix}, \quad 1 < j. \tag{3.13}$$

For instance, the second- and third-order corrections are

$$\mathbf{s}_2 = \frac{F}{\tau^2} \begin{pmatrix} \dfrac{1}{4\cos\theta}(F + 2\xi F') \\ \dfrac{3}{2B} F' \end{pmatrix}, \tag{3.14}$$

$$\mathbf{s}_3 = \frac{3F}{8B\tau^3} \begin{pmatrix} \dfrac{1}{\cos\theta}\left[2\xi(F')^2 + F(2F' + \xi F'')\right] \\ \dfrac{3}{B}\left[2(F')^2 + FF'\right] \end{pmatrix}, \tag{3.15}$$

where the prime denotes the differential operator with respect to ξ. As in the linear case, higher-order eigenvectors impose a specific relation between the amplitude of the perturbation velocity and height at $\tau = 1$. Therefore, the initial condition (3.5) compatible with the actual solution is uniquely determined by substituting (3.12), (3.14) and (3.15) into (3.6), evaluating the ensuing expressions at $\tau = 1$ and identifying coefficients of the same order in υ with those in expansion (3.5). We omit the details here for the sake of brevity.

In order to give a criterion for the validity of the present linear stability analysis, we enforce the condition $\|\mathbf{s}_1\| \gg \upsilon\|\mathbf{s}_2\|$ in the velocity field at $\tau = 1$, i.e.

$$2B \gg 3\upsilon|F'|. \tag{3.16}$$

In such a case, from (3.12), (3.14) and (3.15), we find that the perturbation $\mathbf{s}$, independent of its initial shape, is attenuated along the ray $\xi = \text{constant}$. Otherwise, nonlinear effects become important during the initial stage, and the linear decay rate is not an accurate measure of the attenuation factor except at late time.

The simplest case, a small sinusoidal disturbance with amplitude υ at $\tau = 1$, defined by the function

$$F(\xi) = \mathrm{e}^{a_0\xi i}, \quad 0 \leqslant \xi \leqslant X_s(t_c), \tag{3.17}$$

exhibits, according to its linear solution (3.12), a decay rate independent of its initial wavelength $\lambda_0 = 2\pi/a_0$. Its amplitude decreases as time proceeds at the rate $1/\tau$, and its wavelength increases linearly with time. Substituting (3.17) into (3.16), we find that this conclusion is valid when the initial wavelength of the disturbance is large enough, i.e. $\lambda_0 \gg 3\pi\upsilon/B$.

We notice that non-uniform time-dependent effects of the background flow stabilize the kinematic wave. The well-known stability criterion for plane-parallel flows at high Reynolds number – 'the basic flow is critically stable for any wavelength when $Fr_p = 2$' (Jeffreys 1925) – differs abruptly from that resulting for kinematic waves, which shows that small disturbances are stable independent of their initial shape. Furthermore, stable waves lengthen as they are convected downstream, whilst they remain with constant wavelength in the plane-parallel case (e.g. Jeffreys 1925). These results also differ from that previously reported by Lighthill & Whitham (1955) because of the influence of base-flow spatio-temporal gradients on the behaviour of

small disturbances. Finally, the present solution serves in the next sections to quantify the accuracy of near-parallel stability results (§ 3.2) and to validate a numerical code that solves the full shallow-water equations (§ 3.3).

3.2. *Linear stability analysis by means of multiple scales*

We have seen in § 2 how the basic flow, constituted by the kinematic wave, travels along one family of characteristic curves defined in the $\{\hat{x}, \hat{t}\}$-plane. The hydrodynamic instabilities that develop under such base state move however along two families of real characteristic curves, defined by the partial differential equations (2.1)–(2.3) in the $\{X, t\}$-plane:

$$\frac{\mathrm{d}X}{\mathrm{d}t} = U \pm \sqrt{\eta \cos\theta}. \tag{3.18}$$

In order to include these phenomena in the formulation of the stability problem, it is necessary to apply the multiple-scale technique (e.g. Schmid & Henningson 2001). This approach derives an evolution equation for the slowly varying amplitude of the perturbations going at high order (i.e. the order next to the linear one), and it is likely to be valid in the vicinity of a neutral state. In this section, we derive a linear stability criterion based on multiple scales with corrections to the first order coming from the second-order linear terms. So, we avoid the tedious task of solving the full second-order correction term. Formally, a near-parallel stability formulation results from this approach that is no longer restricted to the case $Fr_p = 2$.

To this end, we expand the perturbed flow $[\eta, U]^T$ with respect to its ϵ-dependence in the form

$$\eta(X, t; \epsilon) = H_0(\hat{x}, \hat{t}) + \epsilon h(\hat{x}, \hat{t}, X, t; \epsilon) + O(\epsilon^2), \tag{3.19}$$

$$U(X, t; \epsilon) = V_0(\hat{x}, \hat{t}) + \epsilon u(\hat{x}, \hat{t}, X, t; \epsilon) + O(\epsilon^2). \tag{3.20}$$

Substituting (3.19)–(3.20) into (2.1)–(2.2), taking into account (2.5) and (2.8)–(2.11), and neglecting terms $O(\epsilon^2)$ except those involving gradients of the base flow, one is left with the following linear equations for the perturbations:

$$\frac{\partial \boldsymbol{s}_1}{\partial t} + \boldsymbol{A} \cdot \frac{\partial \boldsymbol{s}_1}{\partial X} + (\boldsymbol{B} + \epsilon \boldsymbol{C}) \cdot \boldsymbol{s}_1 = \boldsymbol{F}, \tag{3.21}$$

where

$$\boldsymbol{A} \equiv \begin{pmatrix} V_0 & \dfrac{f V_0^2}{8 \sin\theta} \\ \cos\theta & V_0 \end{pmatrix}, \quad \boldsymbol{B} \equiv \begin{pmatrix} 0 & 0 \\ -\dfrac{8(\sin\theta)^2}{f V_0^2} & \dfrac{2 \sin\theta}{V_0} \end{pmatrix}, \tag{3.22}$$

$$\boldsymbol{C} \equiv \begin{pmatrix} \dfrac{\partial V_0}{\partial \hat{x}} & \dfrac{f V_0}{4 \sin\theta} \dfrac{\partial V_0}{\partial \hat{x}} \\ \dfrac{2 \cos\theta(f - 2\tan\theta)}{f V_0} \dfrac{\partial V_0}{\partial \hat{x}} & \dfrac{\partial V_0}{\partial \hat{x}} \end{pmatrix}, \quad \boldsymbol{F} \equiv \begin{pmatrix} 0 \\ \dfrac{2\tan\theta - f}{4 \tan\theta} V_0 \dfrac{\partial V_0}{\partial \hat{x}} \end{pmatrix}. \tag{3.23}$$

The systems of partial differential equations (3.9)–(3.11) and (3.21)–(3.23) are exactly the same, with the only difference that converse to the former case, matrices $\boldsymbol{A}$–$\boldsymbol{C}$ do not depend on X and t. The analogy between both analyses is possible, since we have retained the higher-order correction $\epsilon\boldsymbol{C}$ in the multiple-scale formulation. If one neglects this term (see below), one obtains the same stability result as for the plane-parallel flow, which is qualitatively different from the exact one (§ 3.1). As a matter of fact, this is what Lighthill and Whitham did when they derived the

'telegraph equation' (see Lighthill & Whitham 1955, pp. 294–295). So the main new features of the present analysis are that non-parallel time-varying effects originating from the slow streamwise variations of the background flow are taken into account.

Since matrices A–C do not depend on the independent variables X and t, the solution to the linear equations (3.21) now admits a decomposition in normal modes in the rapid scale $\{X, t\}$. Hence, we apply the Laplace transform in $X \in [0, \infty)$ to (3.21), which yields

$$\frac{\partial S_1}{\partial t} + D \cdot S_1 = \frac{1}{s} F \quad \text{with} \quad D \equiv As + B + \epsilon C \tag{3.24}$$

and

$$S_1(s, t) = \int_0^\infty e^{-sX} s_1(X, t) \, dX, \quad s \in \mathbb{C}. \tag{3.25}$$

The solution to (3.24) can be written as

$$S_1(s, t) = (V \cdot E \cdot V^{-1}) \cdot S_1^o + s^{-1} V \cdot (E - I) \cdot \Lambda^{-1} \cdot V^{-1} \cdot F, \tag{3.26}$$

where $S_1^o(s)$ denotes the initial condition at $t = 0$; $E \equiv \exp(t\Lambda)$ arises from the eigenvalue decomposition of D (i.e. $D = -V \cdot \Lambda \cdot V^{-1}$); and V are the eigenfunctions of D in columns. We start analysing the response to the initial conditions, and later we shall study the particular solution that includes the constant vector F.

3.2.1. *Response to initial conditions*

To characterize the stability of the response to the initial condition S_1^o, a measure of the amplification $G(s, t)$ is required (Schmid & Henningson 2001),

$$G(s, t) = \frac{\|S_1(s, t)\|^2}{\|S_1^o(s)\|^2} = \|V \cdot E \cdot V^{-1}\|^2. \tag{3.27}$$

In the present study, to characterize the amplification of disturbances, we use the least stable mode of $-D$, which gives

$$G(s, t) = \|V \cdot E \cdot V^{-1}\|^2 = \exp\{2 \max[\text{Re}(\hat{\lambda}_+)]t\}. \tag{3.28}$$

Thus, the stability of our dynamic system is governed by the real part of the least stable eigenvalue that appears in the diagonal matrix Λ,

$$\Lambda = \begin{pmatrix} \hat{\lambda}_+ & 0 \\ 0 & \hat{\lambda}_- \end{pmatrix}, \quad \hat{\lambda}_\pm \equiv \frac{\sin \theta}{2V_0} \lambda_\pm, \tag{3.29}$$

with

$$\lambda_\pm = -\{2(1 + a + \phi) \pm \sqrt{2}\sqrt{2 + 2a^2\varrho - 4\phi + (8\varrho - 2)\phi^2 + a[(8\varrho - 1)\phi - 2]}\}, \tag{3.30}$$

in which ϕ is the local free-surface slope of the base solution defined by (2.21); ϱ is a measure of the plane-parallel Froude number, given by (2.22); and the non-dimensional, complex, wavenumber a is defined as

$$a \equiv \frac{sV_0^2}{\sin \theta} = \gamma + i\alpha. \tag{3.31}$$

The real and imaginary parts of $\hat{\lambda}_\pm$ are the exponential growth rate and the temporal frequency, respectively. On the other hand, the real part γ is the spatial growth rate (we set $\gamma = 0$ hereafter in order to perform a temporal stability analysis; Gaster 1962), and the imaginary part α is the local wavenumber. The reader must note that
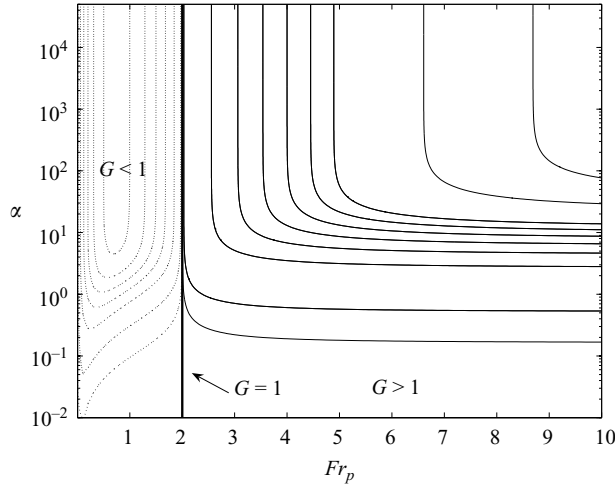
FIGURE 3. The contour lines of the constant growth/decay rate in the $\{Fr_p, \alpha\}$-plane for the plane-parallel flow. Continuous lines: $\mathrm{Re}(\lambda_-) = 0$, 0.001, 0.01, 0.2, 0.4, 0.6, 0.8, 1, 1.2, 2, 3. Dashed lines: $\mathrm{Re}(\lambda_-) = -0.001$, -0.01, -0.05, -0.1, -0.15, -0.2, -0.25.

$\mathrm{Re}(\lambda_-) > \mathrm{Re}(\lambda_+)$, and thus λ_- must define the operator $G(s, t)$. Hence, the neutral curve for instability, corresponding to $\mathrm{Re}(\lambda_-) = 0$ (i.e. $G(s, t) = 1$), is easily obtained by substituting $a = \mathrm{i}\alpha_{cr}$ into (3.30). Solving for α_{cr}, it yields

$$\alpha_{cr}^2 = \frac{32\phi(1 + \phi)^2(2 + \phi - 2\varrho\phi)}{64\varrho^2\phi^2 + (2 + \phi)^2 - 16\varrho(1 + 4\phi + 2\phi^2)}. \tag{3.32}$$

Before undertaking the analysis of the near-parallel stability results of a kinematic wave down an open inclined channel, it is convenient to consider first the simplest case of a uniform flow, thus reproducing previously known stability results. This analysis will also serve as a reference that will help to understand the near-parallel results. For a uniform and steady basic flow, $H_0 = \text{constant}$ and $V_0 = \text{constant}$, one has $\partial V_0 / \partial \hat{x} = 0$ in (3.23) and $\phi = 0$. Hence, $\boldsymbol{C}$ and $\boldsymbol{F}$ vanish. The eigenvalues $\lambda_\pm$ for this simplified case are obtained setting $\phi = 0$ in (3.30), which yields

$$\lambda_\pm = -2[(1 + a) \pm \sqrt{1 + a^2\varrho - a}]. \tag{3.33}$$

The neutral curve for instability is readily obtained by following the same procedure as indicated above. Indeed, setting $a = \mathrm{i}\alpha$ in (3.33), it reads

$$\lambda_\pm = -2\left\{1 \pm \sqrt{2}\sqrt{1 - \varrho\alpha^2 + \sqrt{\alpha^2 + (\varrho\alpha^2 - 1)^2}}\right.$$
$$\left. + \mathrm{i}[\alpha \mp \sqrt{2}\sqrt{\varrho\alpha^2 - 1 + \sqrt{\alpha^2 + (\varrho\alpha^2 - 1)^2}}]\right\}. \tag{3.34}$$

It is an easy exercise to show that the real part of λ_- vanishes at all wavenumbers α when $\varrho = 1/4$ (i.e. $Fr_p = 2$). The flow is stable ($G(s, t) < 1$) for $\varrho > \varrho_{cr} = 1/4$ (i.e. $Fr_p < 2$), whilst it is (convectively) unstable ($G(s, t) > 1$) for any value of the wavenumber α if $\varrho < 1/4$ (i.e. $Fr_p > 2$). The convective nature of the instability is due to the supercritical regime of the background flow. This obviously reproduces the instability condition $Fr_p > 2$ of Jeffreys (1925): any perturbation is unstable above the critical Froude number that is equal to 2. Figure 3 depicts the neutral curve
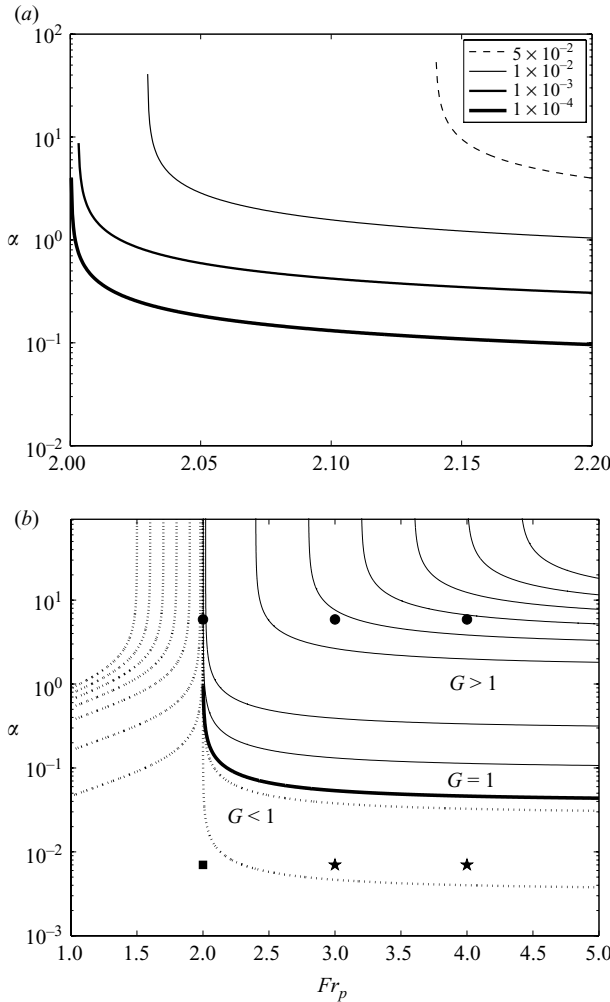
FIGURE 4. (a) Neutral curves for different values of $\phi > 0$; (b) the contour lines of the constant growth/decay rate $\text{Re}(\lambda_-)$ in the $\{Fr_p, \alpha\}$-plane for $\phi = 10^{-4}$. Continuous lines: $\text{Re}(\lambda_-) = 0$, 0.001, 0.01, 0.2, 0.4, 0.6, 0.8, 1, 1.2. Dotted lines: $\text{Re}(\lambda_-) = -0.0001, -1.985 \times 10^{-4}, -0.001, -0.01, -0.05, -0.1, -0.15, -0.2, -0.25$.

in the $\{Fr_p, \alpha\}$-plane, which is just the vertical straight line $Fr_p = 2$, together with some contour lines for the constant growth/decay rate. Note that for Fr_p close to the critical value $Fr_{cr} = 2$ the growth rate is so small that an extremely long channel would be required for the developments of the unstable waves.

Figure 4(a) shows the neutral curves in the $\{Fr_p, \alpha\}$-plane for several values of $\phi > 0$. As is observed in this figure, there are marked differences with the neutral curve for the parallel flow case $\phi = 0$ (i.e. with the vertical line $Fr_p = 2$ in figure 3). Firstly, the flow is always stable independent of the Froude number for very small wavenumbers, i.e. for $\alpha < \alpha_\infty(\phi)$:

$$\alpha_\infty \equiv \lim_{\varrho \to 0} \alpha_{cr} = \sqrt{\frac{32\phi(1 + \phi)^2}{2 + \phi}}. \tag{3.35}$$
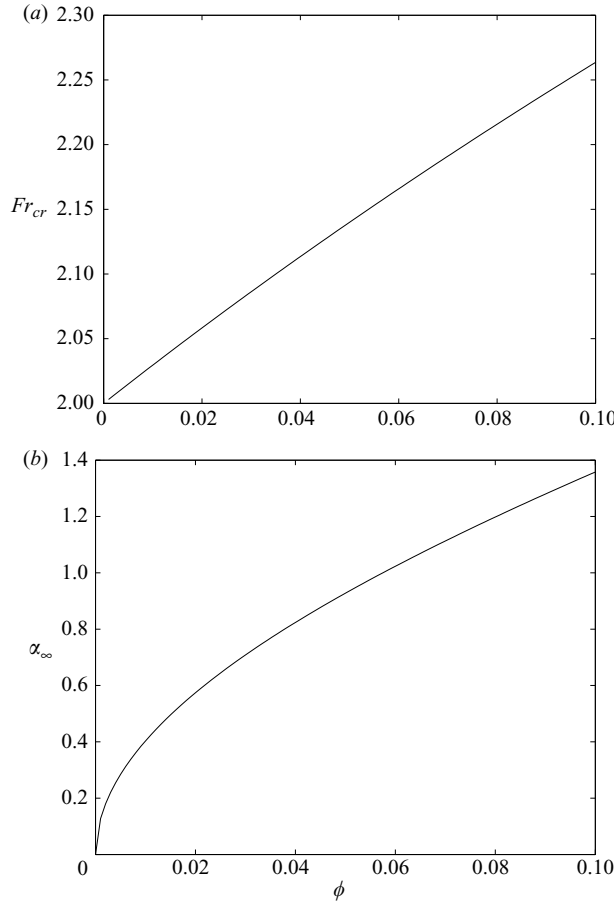
FIGURE 5. (*a*) Fr_{cr} and (*b*) α_{∞} as functions of $\phi > 0$.

Secondly, the minimum, or critical, Froude number for instability (which defines the vertical asymptotes in figure 4*a*),

$$Fr_{cr}(\phi) \equiv \left[\frac{8\phi^2}{1 + 4\phi + 2\phi^2 - (1 + \phi)\sqrt{1 + 6\phi + 3\phi^2}} \right]^{1/2}, \qquad (3.36)$$

is always larger than 2 when $\phi > 0$. This critical Froude number tends to 2 as $\phi \to 0$, though the wavenumber α_{∞} also vanishes. As in the parallel case, the flow is unstable for almost any wavenumber when $Fr_p > Fr_{cr}$ (except for very small wavenumbers, as commented above). To have an idea of the most unstable wavenumbers, figure 4(*b*) shows the contour lines of the constant growth/decay rate for a particular value of ϕ. It is observed that the critical Fr_p is much larger than 2 for low wavenumbers, and the growth rate is quite small, bordering the neutral curve for $Fr_p > Fr_{cr}$. For very high wavenumbers, the critical Fr_p may also be larger than 2, with a growth rate not so large. But these very high wavenumbers, like the very small ones, are too extreme to be physically meaningful. Thus, the critical values $\{Fr_{cr}, \alpha_{\infty}\}$ are the most significant physical results. Figure 5 shows these critical values as functions of $\phi \geqslant 0$.
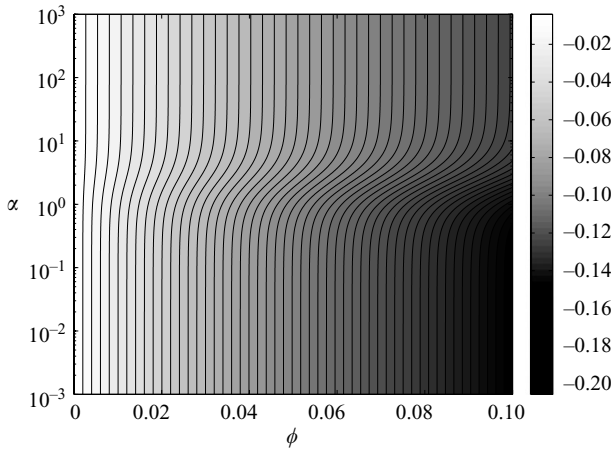
FIGURE 6. The contour lines of constant growth rate $\text{Re}(\lambda_-)$ in the $\{\phi, \alpha\}$-plane for $Fr_p = 2$.

For $\alpha < \alpha_\infty$ the flow is stable for any Froude number, even Froude numbers larger than 2.

The present result qualitatively agrees with that obtained in the previous section: the flow is stable for any wavenumber when the Froude number of the background flow is 2, i.e. $f = 2 \tan \theta$. In this case, the vector **F** vanishes (see (3.23)), and there is no particular solution to be found. The stability of the system is therefore governed purely by the response to the initial conditions already analysed. Going further to quantify the influence of the multiple-scale hypothesis in the linear stability results, the solution of the particular case $Fr_p = 2$ may serve as the benchmark case to compare with the exact results in §3.1.

Setting $\varrho = 1/4$ in (3.30), the exponential decay rate corresponding to the real part of λ_- (the least stable mode) reads

$$
\text{Re}(\lambda_-) = -\frac{1}{\sqrt{2}} \left[\sqrt{8}(1+\phi) - \sqrt{4 - \alpha^2 - 8\phi + \sqrt{\alpha^4 + 16(1 - 2\phi)^2 + 4\alpha^2(2 + \phi^2)}} \right],
$$
(3.37)

which is plotted in figure 6. Its dependence on the wavelength is negligible for very small and high wavelengths, as is shown by the vertical asymptotes for $\alpha \to \infty$ and 0, respectively. For wavelengths of order unity, the decay rate is influenced substantially by the value of α; the larger the ϕ, the stronger the dependence. Regarding (2.22), the near-parallel results are likely to become increasingly valid as ϕ decreases towards zero. For this reason, the focus of the comparison with the exact results is next done in this limit. Expanding (3.37) with respect to $\phi = 0$, neglecting terms $O(\phi^2)$, taking into account (3.29) and substituting into (3.28), the amplification factor reads

$$
G(\alpha, t) \approx \exp\left[-\frac{m(\alpha)\sin\theta}{2V_0}\phi t + O(\phi^2) \right] \quad \text{with} \quad m(\alpha) \equiv \frac{32 + 6\alpha^2}{4 + \alpha^2}.
$$
(3.38)

Substituting the definition of ϕ (2.21) into the equation shown above, and expanding in powers of $T \equiv -Bt/(1 + Bt)$ with respect to $T = 0$, the amplification factor is

rewritten as

$$G(\alpha, t) \approx 1 - \frac{m(\alpha)}{3} \frac{Bt}{1 + Bt} + O\left[\left(\frac{Bt}{1 + Bt}\right)^2\right]. \tag{3.39}$$

Besides, the Laplace transform in X of $F[\xi(X, t)]$, denoted by $\mathbb{L}[F](s, t)$, is related with its Laplace transform in ξ, denoted by $\mathbb{L}[F](s)$, by the following relation:

$$\mathbb{L}[F](s, t) \equiv \int_0^\infty F(\xi) e^{-sX} dX = \tau \int_0^\infty F(\xi) e^{-s\tau\xi} d\xi = \tau \mathbb{L}[F](s\tau). \tag{3.40}$$

Thus, the amplification factor associated to the exact solution $\mathbf{s}_1$ (see (3.12)) is

$$G(\alpha, t) = \frac{\|\mathbb{L}[\mathbf{s}_1](s, t)\|^2}{\|\mathbb{L}[\mathbf{s}_1](s, 0)\|^2} = \left|\frac{\mathbb{L}[F](s\tau)}{\tau \mathbb{L}[F](s\tau)}\right|^2 = 1 - \frac{2Bt}{1 + Bt} + \left(\frac{Bt}{1 + Bt}\right)^2. \tag{3.41}$$

Comparing (3.39) and (3.41), and regarding that the value of $m(\alpha)$ ranges between 6 and 8 when the wavenumber α varies from 0 to ∞, the error intrinsic to the multiple-scale analysis in the prediction of the linear decay rate at the initial stage ($t \ll 1/B$) decreases from 33 % to 0 % for wavenumbers varying between 0 and ∞, respectively.

3.2.2. *Response to forcing*

Once we have established the stability criterion of the homogeneous part of solution (3.26), i.e. the first term on the right-hand side of (3.26), we proceed to analyse the particular solution $\mathbf{S}_p$, i.e. the second term on the right-hand side of (3.26). This last term can be decomposed into two contributions:

$$\mathbf{S}_p = \mathbf{S}_{pa} + \mathbf{S}_{pb} \tag{3.42}$$

with

$$\mathbf{S}_{pa} \equiv -\mathbf{V} \cdot \mathbf{\Lambda}^{-1} \cdot \mathbf{V}^{-1} \cdot \frac{\mathbf{F}}{s}, \quad \mathbf{S}_{pb} \equiv \mathbf{V} \cdot \mathbf{E} \cdot \mathbf{\Lambda}^{-1} \cdot \mathbf{V}^{-1} \cdot \frac{\mathbf{F}}{s}. \tag{3.43}$$

The first one, $\mathbf{S}_{pa}$, arises from the non-homogeneous part of (3.21) and can be readily rewritten in the original variables (X, t):

$$\mathbf{s}_{pa} = (\mathbf{B} + \epsilon\mathbf{C})^{-1} \cdot \mathbf{F}. \tag{3.44}$$

Since all the terms involved in this equation depend on neither X nor t, $\mathbf{S}_{pa}$ is a steady, uniform solution. Therefore, it is stable.

The second contribution to the particular solution, i.e. $\mathbf{S}_{pb}$, corresponds to a homogeneous solution that was introduced in (3.26) to differentiate the response of the system to the initial conditions $\mathbf{S}_1^o$, i.e. to cancel the contribution of $\mathbf{S}_{pa}$ at $t = 0$. Hence, it represents the temporal evolution of a constant, uniform disturbance. The wavelength of this perturbation is obviously ∞, or $\alpha = 0$, which is, according to the previous analysis, stable for any Froude number.

3.3. *Numerical simulation*

The most significant result found in the previous sections is that the behaviour of small disturbances superimposed on a kinematic wave differs qualitatively from their evolution on a plane-parallel flow under two specific scenarios: first, with $Fr_p = 2$, small-amplitude long-wave disturbances are stable, with a linear decay rate independent of the wavelength and with wavelengths that increase linearly with time; second, for larger Froude numbers (i.e. $Fr_p > 2$) small-amplitude perturbations with wavenumber values below α_∞ are stable. In the first scenario, the asymptotic solution

of nonlinear perturbations is already known, and so we do not need to corroborate the result. Furthermore, the error arising from the multiple-scale analysis has also been quantified. Hence, this case is next used to show the capabilities of the numerical code to compute with accuracy the amplitude, wavelength and phase speed of nonlinear perturbations. Once we have validated the numerical code to solve the nonlinear evolution of small perturbations, we proceed to verify the second result.

We are interested here in solving (2.1)–(2.3) for the flow whose initial condition ($t = 0$) is given by

$$U(X, 0) = \begin{cases} \vartheta X & \text{if } X_{b0} \leqslant X \leqslant X_{b1,} \\ \vartheta X + \upsilon \sin\left[\dfrac{2\pi}{\lambda_0}(X - X_{b1})\right] & \text{if } X_{b1} \leqslant X \leqslant X_{b2}, \\ \vartheta X & \text{if } X_{b2} \leqslant X \leqslant X_{b3,} \end{cases} \quad \eta(X, 0) = \frac{f}{8}\frac{U^2}{\sin\theta},$$

(3.45)

where λ_0 is the initial wavelength of the disturbance; $X_{b0} = X_{b1} - 3\lambda_0 > 0$; $X_{b2} = X_{b1} + n\lambda_0$; and n represents the number of waves introduced as perturbations.

The nonlinear set of equations (2.1)–(2.3) is solved with SharpClaw, the new incarnation of WENOCLAW (Ketcheson & LeVeque 2008), in the computational domain with cells $\mathscr{C}_i = (X_{i-1/2}, X_{i+1/2})$, $i = 1, \ldots, Nx$. The computational variables are $\boldsymbol{Q}_i^n$, which approximate the average value over the ith interval at time t_n:

$$\boldsymbol{Q}_i^n \equiv \begin{pmatrix} \overline{\eta}_i^n \\ \overline{\eta U}_i^n \end{pmatrix} \approx \frac{1}{\Delta X_i} \int_{\mathscr{C}_i} \begin{pmatrix} \eta \\ \eta U \end{pmatrix}(X, t_n)\mathrm{d}X, \quad \Delta X_i = X_{i+1/2} - X_{i-1/2}, \quad (3.46)$$

where the centre of the cell is $X_i = (X_{i+1/2} + X_{i-1/2})/2$. For simplicity we assume a uniform grid with cell size $\Delta X_i = \Delta X$. A component-wise weighted essentially non-oscillatory (WENO) scheme is adopted in the current work. Left- and right-going flux differences are computed using Roe's approximate Riemann solver with entropy fix for transonic rarefactions. The gravitational source term in the momentum balance equation is discretized according to Črnjarić Žic, Vuković & Sopta (2004; note that there is a misprint in the sign of the first component of $\mathbf{l}^{(2)}$ of equation (42) in their paper). To preserve a well-balanced scheme in the kinematic regime, we apply the same source term decomposition to the friction force, which is evaluated from the known values at the cell centres, by using the WENO reconstruction procedure with the smoothness indicators of the water depth variable η. This scheme is only second-order accurate for general solutions based on truncation error analysis (Xing & Shu 2005). However, to the author's knowledge, the code of WENO methods for non-homogeneous problems and moving water (that maintains fifth-order accuracy) is a tedious task, and its formulation has currently been carried out only for ideal flows (Castro, Gallardo & Parés 2006; Noelle, Xing & Shu 2007). Finally, in order to complete the definition of the scheme, we need to introduce the temporal discretization, which has been chosen to be a third-order accurate, strong stability-preserving Runge–Kutta method (denoted by SSPRK(3,3) in Gottlieb, Ketcheson & Shu 2009).

Taking into account that we are interested in analysing supercritical regimes (in particular, $Fr_p \geqslant 2$), two physical BCs are to be imposed at the inlet, and thus no physical outflow BCs are to be applied (e.g. Blayo & Debreu 2005; Bohorquez & Darby 2008). However, additional numerical BCs are required by the numerical scheme (e.g. Shu 2009): for a fifth-order WENO scheme, the five-cell stencil ($\mathscr{C}_{-1}, \mathscr{C}_0, \mathscr{C}_1, \mathscr{C}_2, \mathscr{C}_3$) built using the six-cell interfaces ($X_{-3/2}, X_{-1/2}, X_{1/2}, X_{3/2}, X_{5/2}, X_{7/2}$) is employed at the inlet, whilst the five-cell stencil ($\mathscr{C}_{Nx-2}, \mathscr{C}_{Nx-1},$

$\mathscr{C}_{Nx}, \mathscr{C}_{Nx+1}, \mathscr{C}_{Nx+2}$) built using the six-cell interfaces $(X_{Nx-5/2}, X_{Nx-3/2}, X_{Nx-1/2}, X_{Nx+1/2}, X_{Nx+3/2}, X_{Nx+5/2})$ is employed at the model outlet; since our WENO implementation deals with BCs at the cell interfaces, inflow BCs are obtained by evaluating (3.1) at $X = X_{-3/2}, X_{-1/2}, X_{1/2}$; although numerical outflow BCs have usually been undertaken using the characteristic variable extrapolation (CVE) method (e.g. Blayo & Debreu 2005; Bohorquez & Darby 2008), we find that extrapolation based on asymptotic solutions of the problem under consideration, i.e. (3.1), supersedes CVE, and thus both the water depth $\bar{\eta}$ and the flow rate $\overline{\eta U}$ are extrapolated following a linear and a cubic law in the streamwise coordinate, respectively, at $X = X_{Nx+1/2}, X_{Nx+3/2}, X_{Nx+5/2}$. Next, as discussed in §3.1, the amplitude of the perturbation must satisfy the relation $\upsilon \ll \vartheta \lambda_0/2\pi$ in order to avoid nonlinear effects. So, the multiple-scale results for $Fr_p > 2$ can be compared with the nonlinear numerical simulations.

One should note that the main difference of this numerical technique with respect to that applied by Brook, Falle & Pedley (1999) lies in the BC. Traditionally, roll waves are numerically studied by using their periodicity properties, and so periodic BCs are frequently employed. Hence, in the plane-parallel flow one just needs to solve the physical domain occupied by disturbances. However, in order to analyse the stability of the more general basic flows (which are not periodic) we have to adopt a different approach. This fact introduces an additional difficulty for $Fr_p > 2$, since the exact solution for the background flow is unknown in this case. This requires us to solve at each time step the whole domain travelled by the waves. Close to criticality, i.e. for small growth rate, the length of the domain (X_{b2}, X_{b3}) necessary for us to observe a significant change in the wave amplitude is extremely large, and we shall require unreachable computational resources in order to run such numerical simulations. In addition, the unperturbed background flow is to be computed in order to isolate the nonlinear disturbance from the perturbed flow. The set-up for the background flow is obviously exactly the same as for the perturbed flow but setting $\upsilon = 0$ in (3.45). Therefore, both the perturbed and unperturbed background flows are solved for $Fr_p > 2$ in the entire domain that waves travel, and nonlinear perturbations are obtained by extracting the second solution from the first one.

On the other hand, the case $Fr_p = 2$ is much easier to compute. First, the exact solution is known, and so we just need to solve the perturbed flow. Nonlinear disturbances are then obtained by subtracting the asymptotic background flow (3.1)-(3.2) from the numerical simulation. Second, in order to reduce the computational time, we initially solve in a small region I_1, i.e. $X_{b3} \approx X_{b2}$. Before the wavetrain reaches the end of I_1, a new domain I_2 is defined that contains the subregion in which waves exist (denoted as $I_\cap$ in figure 7), and it is enlarged downward adding new nodes (subdomain I_3) which are initialized to the values defined by (3.1)–(3.2). This process is repeated several times during the numerical simulation. Thus, we solve at nearly each time step the small domain in which the waves are located.

Before undertaking the analysis of the numerical results, we notice that the initial value of α for the base state, i.e. for (3.45) with $\upsilon = 0$, which is obtained by setting $s = \mathrm{i}\, 2\pi/\lambda_0$ in (3.31), is

$$\alpha^o(X) \equiv \alpha(X, 0) = \frac{2\pi}{\lambda_0} \frac{U(X, 0)^2}{\sin\theta} = \frac{2\pi}{\lambda_0} \frac{(\vartheta X)^2}{\sin\theta} \qquad (3.47)$$

and varies between

$$\alpha^o_{min} \equiv \frac{2\pi}{\lambda_0} \frac{(\vartheta X_{b1})^2}{\sin\theta} \quad \text{and} \quad \alpha^o_{max} \equiv \frac{2\pi}{\lambda_0} \frac{[\vartheta(X_{b1} + n\lambda_0)]^2}{\sin\theta}. \qquad (3.48)$$
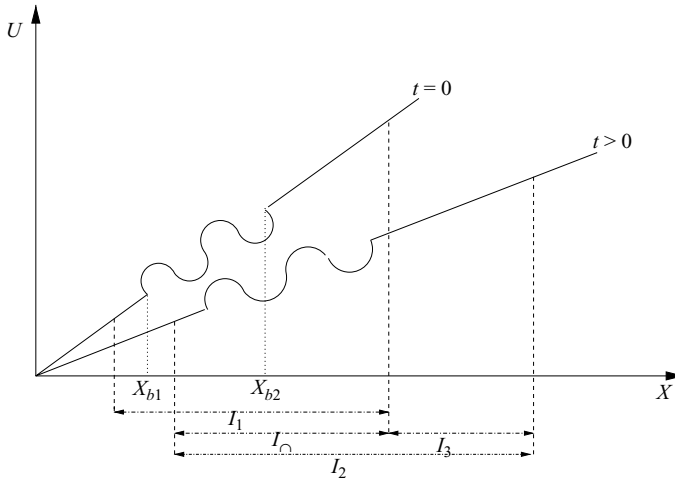
FIGURE 7. Sketch of the initial condition at $t = 0$ for the velocity field U according to the numerical experiment defined in §3.3.

Similarly, the initial value of ϕ,

$$\phi^o(X) \equiv \phi(X, 0) = \frac{U(X, 0)}{\sin \theta} \frac{\partial U}{\partial X}(X, 0) = \frac{\vartheta^2 X}{\sin \theta}, \qquad (3.49)$$

varies between the range of values

$$\phi^o_{min} \equiv \frac{\vartheta^2 X_{b1}}{\sin \theta} \quad \text{and} \quad \phi^o_{max} \equiv \frac{\vartheta^2 (X_{b1} + n\lambda_0)}{\sin \theta}. \qquad (3.50)$$

Therefore, the local, linear growth rate (3.28)–(3.30) varies when it is evaluated for the pair of values $\{\alpha^o_{min}, \phi^o_{min}\}$ and $\{\alpha^o_{max}, \phi^o_{max}\}$, although this effect is negligible when $2\pi\upsilon/\vartheta \ll \lambda_0 \ll X_{b1}$. Furthermore, as the disturbance is convected, the values of ϕ and α, as well as the wavelength, change because of low spatio-temporal variations of the background flow. We observe below that the predictions of the multiple-scale theory based on the initial values $\{\alpha^o_{min}, \phi^o_{min}\}$ and $\{\alpha^o_{max}, \phi^o_{max}\}$ are in close agreement with the numerical growth rates, and we shall conclude that smooth variations of ϕ and α during the numerical simulation do not affect significantly the predictions of the multiple-scale theory.

The result of the numerical simulation for $Fr_p = 2$ is in close agreement with the asymptotic solutions obtained in previous sections (see figure 8). By definition, the numerical wavelength shown in figure 8(b) has been determined by considering the distance between consecutive corresponding points of the same phase, such as crests, troughs or zero crossings. Figures 8(a) and 8(b) depict the evolution of the amplitude and wavelength of the disturbances, respectively, normalized with respect to their initial values, which reproduce with accuracy the asymptotic solution (3.12) for

$$F(\xi) = \begin{cases} \sin\left[\dfrac{2\pi}{\lambda_0}(\xi - X_{b1})\right] & \text{if } X_{b1} \leqslant \xi \leqslant X_{b2}, \\ 0 & \text{otherwise.} \end{cases} \qquad (3.51)$$

Moreover, by comparison of the simulated perturbations (figure 8c) and their asymptotic solution (figure 8d), we find out that the phase speed of the waves is
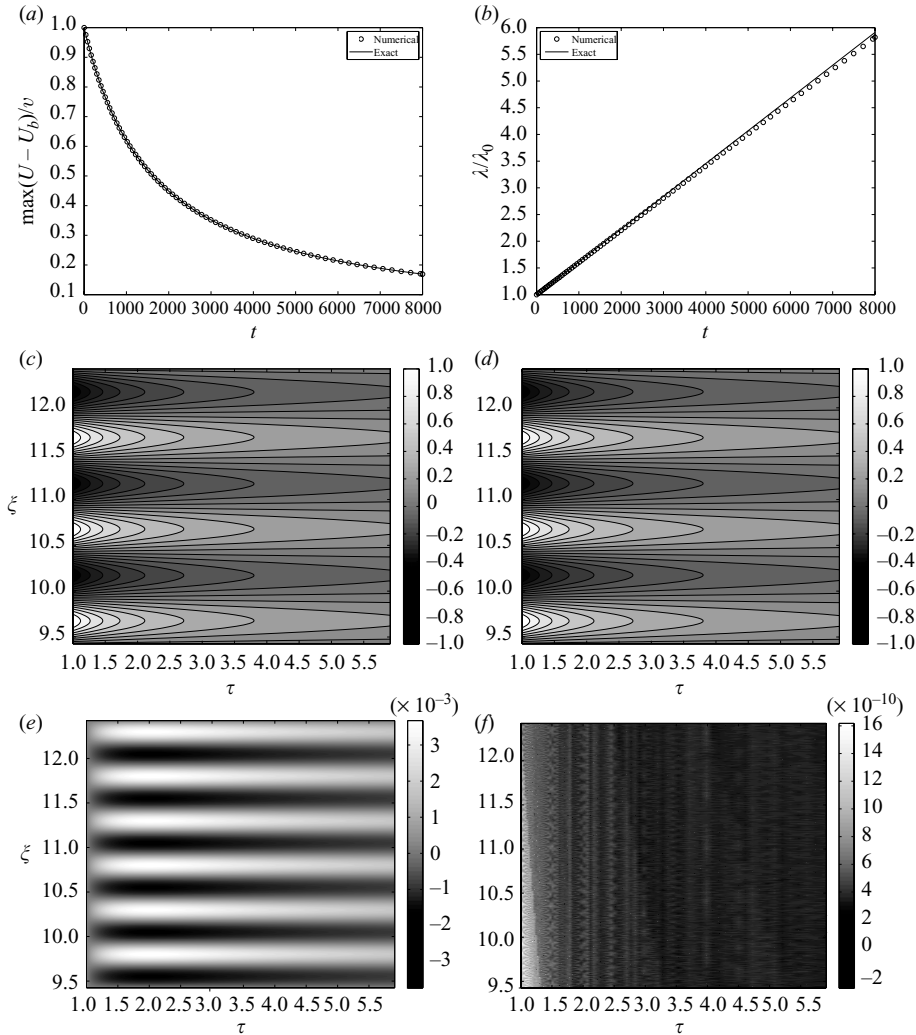
FIGURE 8. Comparison between nonlinear numerical and linear analytical solutions of the disturbance velocity: (a) amplitude and (b) wavelength, normalized with respect to their initial values, as a function of time t; isocontours of (c) nonlinear numerical and (d) linear analytical perturbations in the $\{\tau, \xi\}$-plane, normalized with respect to υ; (e) shows the difference between (c) the computed and (d) the analytical solution; finally, (f) depicts the error in the computation of the background flow with respect to the analytical solution (3.1)–(3.2), i.e. $(U_{b,num} - U_b)/U_b$. The numerical experiment is defined by the values: $\vartheta \approx 4.1 \times 10^{-4}$, $X_{b1} = 9.425$, $X_{b2} = 12.425$, $\upsilon \approx 2 \times 10^{-6}$, $\lambda_0 = 1$, $\theta = 1°$ and $Fr_p = 2$. The computations were conducted with 75×10^3 nodes (corresponding to 1000 nodes per wave at $t = 0$) and $CFL = 0.4$.

also computed with precision. Indeed, absolute errors in the normalized waves are lower than 5×10^{-3} during the simulation (see figure 8e). To conclude the validation, we point out the accuracy of our computations of the base flow, since relative errors lie below 10^{-9} (as shown in figure 8f) – note the noisy aspect of the signal because of the inevitable truncation in the data storage.
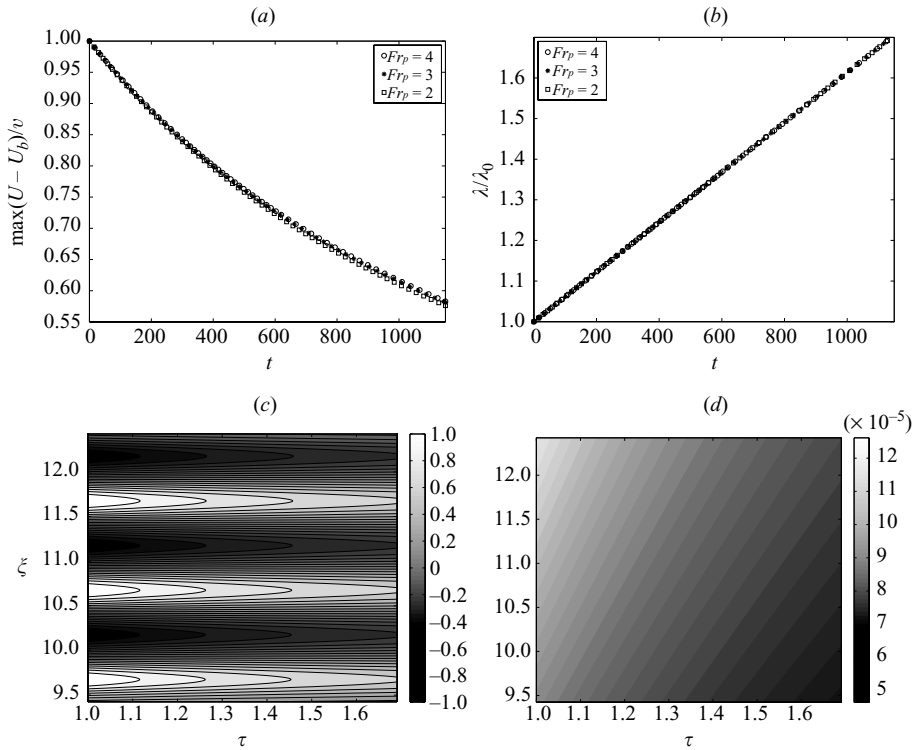
FIGURE 9. Numerical results of the normalized (*a*) amplitude and (*b*) wavelength of the velocity perturbation for three values of the Froude number ($Fr_p = 2, 3, 4$). The retrodicted disturbance of the velocity is also shown in (*c*), as well as the values of ϕ (*d*) based on the numerical simulation in the particular case $Fr_p = 4$. The numerical experiments were conducted under the same conditions as in figure 8.

We are now in a condition to verify that waves with $\alpha^o < \alpha_\infty$ are also stable for $Fr_p > 2$. To this end, the Froude number is increased up to 4, maintaining constant the values of the other parameters. Substituting the values that define the numerical simulations shown in figures 8 and 9 (i.e. $\lambda_0 = 1$, $\theta = 1°$, $\vartheta = 4.1 \times 10^{-4}$, $X_{b1} = 9.425$, $n = 3$) into (3.48), we obtain that α^o varies in the narrow range 0.0054–0.0093. From (2.22), for these values of the Froude number the base flow can be approximated by a kinematic wave if $\phi \ll 2.7$. This restriction is readily satisfied in the present scenario where $\phi \approx O(10^{-4})$ (see below). Hence, the value of ϕ does not depend on the Froude number, and the stability diagram (figure 4*b*) is common to the three simulations. So we have marked the near-parallel stability diagram (figure 4*b*) with a filled square in order to depict the initial location of the numerical experiment for $Fr_p = 2$, whilst we have marked in filled stars the cases $Fr_p = 3, 4$. A check of the normalized amplitude of the wave for $Fr_p = 2, 3, 4$ (see figure 9*a*) shows that the decay rate decreases very slowly when the Froude number grows above 2. Figures 9(*b*) and 9(*c*) illustrate that the wavelength of the perturbation and the wave trajectories evolve identically in the three simulations; i.e. stable disturbances are convected along the expansion fan $\xi = $ constant. As a matter of fact, this result is in agreement with the asymptotic solution (A 7). Therefore, the leading-order velocity of the background flow (2.24) and its gradient can be written as functions of ξ and τ as for $Fr_p = 2$

(see (3.1)–(3.3)),

$$V_0(\xi, \tau) = \vartheta \xi = V_0(\xi), \quad \frac{\partial V_0}{\partial X}(\xi, \tau) = \frac{\vartheta}{\tau} = \frac{1}{\tau} \left.\frac{\partial V_0}{\partial X}\right|_{\tau=1}.$$

Substituting these expressions into the definition of a (3.31) and ϕ (2.21) and taking into account that $s = i2\pi/\lambda$ and $\lambda(\tau) = \lambda_0 \tau$ (e.g. see figure 9b or set $C_1 = F$ into (A 7) with F given by 3.51) yields

$$\alpha(\xi, \tau) = \frac{2\pi[V_0(\xi)]^2}{\lambda(\tau)\sin\theta} = \frac{\alpha^o(\xi)}{\tau}, \tag{3.52}$$

$$\phi(\xi, \tau) = \frac{V_0(\xi)}{\sin\theta}\frac{\partial V_0}{\partial X}(\tau) = \frac{V_0(\xi)\vartheta}{\tau\sin\theta} = \frac{\phi^o(\xi)}{\tau}, \tag{3.53}$$

in which $\alpha^o(\xi)$ and $\phi^o(\xi)$ are given by (3.47) and (3.49), respectively. For completeness, the numerical values of $\phi(\xi, \tau)$ calculated *a posteriori* according to its definition (2.21) are drawn in figure 9(d), verifying the law $\phi(\xi, \tau) \approx \phi^o(\xi)/\tau$ as stated above. Given these temporal tendencies of $\phi(\xi, \tau)$ and $\alpha(\xi, \tau)$, the proof of $\alpha(\xi, \tau) < \alpha_\infty$ (with $\alpha^o(\xi) < \alpha_\infty$) is straightforward (see Appendix B). Finally, we observe from figure 4(b) that the decay rate has a limiting value when increasing Fr_p above 2 with $\alpha = $ constant, which introduces a cutoff in wavenumber for the spectrum, as found in our simulations. The trends are the same for both the multiple-scale stability analysis and the numerical results.

To quantify the accuracy of the linear stability results for the onset of roll waves, we finally present results for disturbances with $\alpha^o > \alpha_\infty$. The same values of the Froude number as before are simulated but decreasing the initial slope of the velocity profile and displacing the location of the waves further downstream, as indicated in the caption of figure 10. This configuration results in α^o (3.48) varying between 5.915 and 5.919, marked with the filled circles in figure 4(b), as ϕ^o (3.50) varies over the range 0.9988×10^{-4} to 0.9992×10^{-4}. A rough estimation of the growth rate, based on the initial conditions of the perturbations, gives (see §3.2) $\text{Re}(2\hat{\lambda}_-) = 0.0489$ with $Fr_p = 3$ and $\text{Re}(2\hat{\lambda}_-) = 0.0758$ with $Fr_p = 4$. Fitting the amplitude of the simulated perturbations (see figures 10(a) and 10(c)), with the law $\log(G(t)) = mt + n$, it follows that $m = 0.0482$ for $Fr_p = 3$ and $m = 0.0752$ for $Fr_p = 4$. The coefficient of determination in both cases is 0.9999. This difference amounts to a 1.5% discrepancy between the growth rate estimated using the linear theory versus nonlinear simulations. This satisfactory result is, in part, due to the smooth variation of ϕ during the numerical simulation (as shown in figure 10d).

3.4. Closure

The aim of this section is to tie the multiple-scale stability results (§3.2) to the appearance of roll waves in the numerical simulation of the dam-break problem (§2). In the original non-dimensional variables $\{X, t\}$, which are related to the slow scale $\{\hat{x}, \hat{t}\}$ by (2.5), the base flow (2.10)–(2.16) and the free-surface slope ϕ (2.21) read

$$H_0 = \frac{f V_0^2}{8\sin\theta}, \quad V_0(X, t) = \frac{2X}{3t} \quad \text{for } 0 \leqslant X \leqslant X_s(t) \equiv \left(\frac{27A\, Fr_p^2\cos\theta}{4}t^2\right)^{1/3}, \quad 0 < t, \tag{3.54}$$

and

$$\phi(X, t) = \frac{V_0}{\sin\theta}\frac{\partial V_0}{\partial X} = \frac{4X}{9t^2\sin\theta} \quad \text{for} \quad 0 < X < X_s(t), \quad 0 < t. \tag{3.55}$$
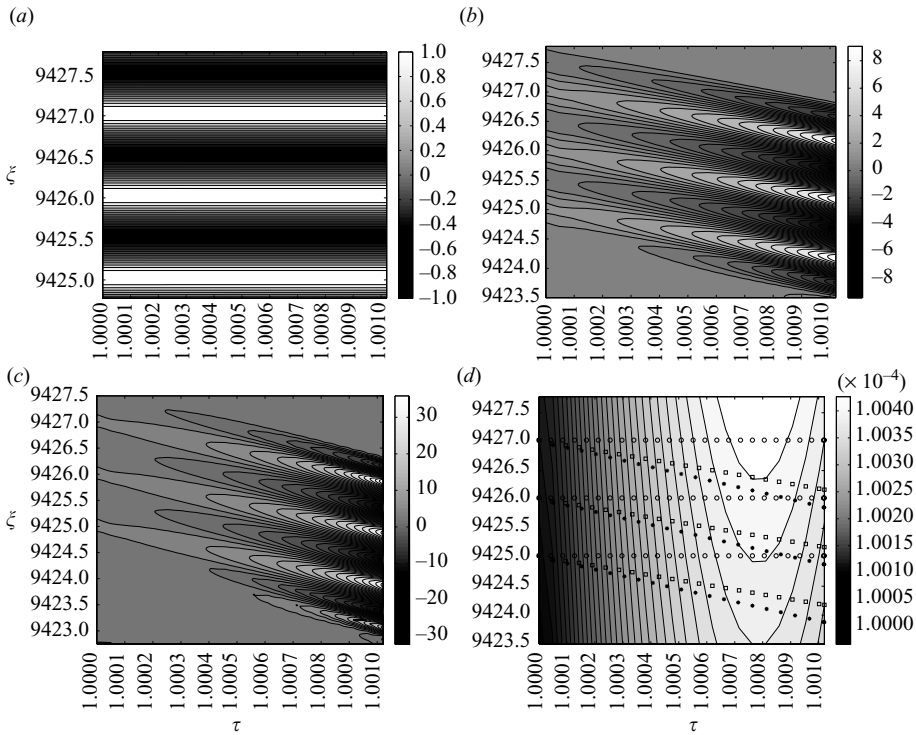
FIGURE 10. The isocontours of the numerically computed perturbations in the $\{\tau, \xi\}$-plane, normalized with respect to υ, for $Fr_p = (a)\ 2,\ (b)\ 3\ (c)\ 4$, respectively. The values of ϕ are also shown in a similar diagram (d), where the trajectories of the wave crests are drawn as the circle, square and asterisk, respectively. The numerical experiment is defined by the values: $\vartheta \approx 1.36 \times 10^{-5}$, $X_{b1} = 9.4248 \times 10^3$, $X_{b2} = 9.4278 \times 10^3$, $\upsilon \approx 3 \times 10^{-8}$, $\lambda_0 = 1$, $\theta = 1°$. The computations were conducted with 75×10^3 nodes (corresponding to 1000 nodes per wave at $t = 0$) and $CFL = 0.2$.

The maximum value of $\phi(X, t)$ at a given time t is attained at the flow front $X_s(t)$,

$$\phi_s(t) = \frac{V_0}{\sin\theta} \left.\frac{\partial V_0}{\partial X}\right|_{X=X_s(t)} = \frac{4}{9t^2 \sin\theta} \left(\frac{27A\, Fr_p^2 \cos\theta}{4} t^2\right)^{1/3}, \quad 0 < t. \tag{3.56}$$

Now, setting $Fr_{cr} = Fr_p$ in (3.36) and writing ϕ as a function of Fr_p, one obtains the critical value of ϕ (denoted hereafter by ϕ_{cr}) that makes the dam-break flow critically stable for a given plane-parallel Froude number Fr_p,

$$\phi_{cr} = \frac{2\left(Fr_p^2 - 2Fr_p\right)}{8 + 4Fr_p - Fr_p^2}. \tag{3.57}$$

It is worth noting that the validity of this result is limited by the kinematic-wave approximation considered to describe the base flow. As stated just below (2.22), the kinematic-wave equation (2.11) by Lighthill & Whitham (1955) is an approximate solution to the shallow-water equations (2.6) and (2.7) only when $\phi \ll \phi^*(Fr_p)$. For instance, substituting the values of $Fr_p = \{2.078, 2.25, 2.814, 5\}$ into (2.22) and (3.57) yields $\phi^* = \{27.15, 9.53, 4.04, 2.38\}$ and $\phi_{cr} = \{0.027, 0.09, 0.40, 10\}$, respectively. We observe that the condition $\phi_{cr} \ll \phi^*$ is satisfied just for Froude numbers slightly

larger than 2, and so the kinematic-wave approximation imposes a strong limitation in the applicability of the stability results. These limitations are further described below.

The critical instant of time (t_{cr}) at which the entire dam-break flow becomes critically stable is obtained by identifying ϕ_{cr} with ϕ_s at $t = t_{cr}$:

$$\phi_s(t_{cr}) = \phi_{cr} \Rightarrow t_{cr} = \left[\frac{2A\left(8 + 4Fr_p - Fr_p^2\right)^3}{27Fr_p(Fr_p - 2)^3 \tan\theta(\sin\theta)^2} \right]^{1/4} \quad \text{for} \quad 2 < Fr_p \ll 5.4641.$$

$$(3.58)$$

This result is likely to be valid for restricted values of the Froude number Fr_p. As a matter of fact, since it is based on the kinematic-wave approximation, (2.22) should be satisfied. Introducing the same tolerance Φ as for the characteristic time t_c (see (2.17)), (2.22) reads

$$\phi_{cr}(Fr_p) < \Phi \left| \frac{2Fr_p^2}{Fr_p^2 - 4} \right|. \tag{3.59}$$

Substituting (3.57) into (3.59), identifying the left- and right-hand sides and solving for Fr_p with several values of the tolerance yields $Fr_p = \{2.078, 2.25, 2.814\}$ for $\Phi^{-1} = \{1000, 100, 10\}$, respectively. Similarly, for the value of $\Phi = 4.25 \times 10^{-3}$ set in §2, we find that the critical time (3.58) is just valid for Froude numbers slightly larger than 2, say $2 < Fr_p \leqslant Fr_p^* \equiv 2.1626$. Conversely, for $Fr_p > Fr_p^*$ the linear theory predicts the formation of roll waves in the entire dam-break flow before the kinematic regime is approached. In particular, for $Fr_p = 5.4641$ the critical time is $t_{cr} = 0$. However, we have to wait until t_c (see (2.17)),

$$t_c = \Phi^{-3/4} \sqrt{\frac{1}{\sin\theta}} \left(\frac{2A\left(\left|Fr_p^2 - 4\right|\right)^3 \tan\theta}{27Fr_p^2} \right)^{1/4}, \tag{3.60}$$

to approach the kinematic-wave solution and thus to apply the linear stability analysis. As commented on in §2, this is the main mathematical drawback of the present results that might be caused by neglecting both higher-order terms of the base flow (2.8)–(2.9) and the non-modal nature of instability waves in the stability analysis. Furthermore, the panorama becomes much more complex in the absence of analytical (or asymptotic) solutions for the frictional dam-break problem on an inclined plane at short and moderate times. On the other hand, from the physical point of view, roll waves in floods on inclines have been uniquely observed in extremely steep slope channels but not over shallow slopes that would require, according to actual results, an extremely long distance for the developments of the waves.

The ratio between t_{cr} (3.58) and t_c (3.60), shown in figure 11 for $\Phi = 4.25 \times 10^{-3}$, is

$$\frac{t_{cr}}{t_c} = \left(\frac{\Phi^3}{\tan^2\theta} \right)^{1/4} \left[\frac{Fr_p\left(Fr_p^2 - 4Fr_p - 8\right)^3}{(Fr_p - 2)^6(Fr_p + 2)^3} \right]^{1/4} \quad \text{for} \quad 2 < Fr_p \ll 5.4641. \tag{3.61}$$

As stated above, this result is formally valid for $2 < Fr_p \leqslant Fr_p^*$ – the limiting value is illustrated in figure 11 with the vertical straight line $Fr_p = Fr_p^*$. Dam-break flows over shallow slopes of the bottom bed, $\theta < 15°$, may first approach the kinematic-wave solution during the period of time $t_c < t < t_{cr}$, later attaining the unstable regime at $t \geqslant t_{cr}$. Therefore, from the present hydraulic linear theory we figure out that when $2 < Fr_p \leqslant Fr_p^*$, the kinematic-wave solution would be observed in reality only on
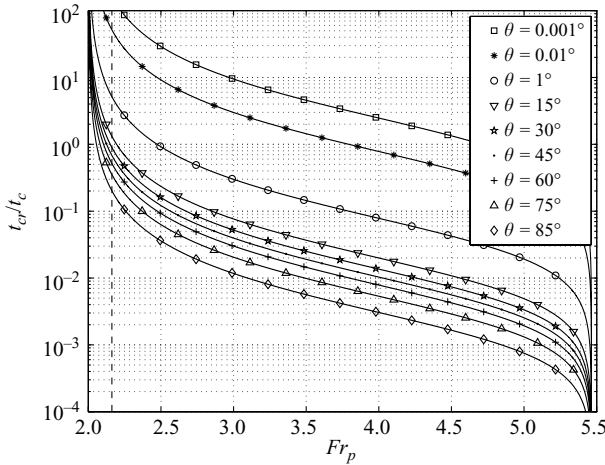
FIGURE 11. The ratio between the critical (t_{cr}) and characteristic (t_c) time, given by (3.61), for $\Phi = 4.25 \times 10^{-3}$ and several bottom slopes.

shallow-slope terrains. Conversely, for larger values of the bed slope, i.e. $\theta > 15°$, we find that the entire flow field can be unstable at $t < t_c$, and so the growth could arise from developments in the time before t_c. The present study predicts the critical time for the onset of roll waves only in the former case.

The next point to address is the characterization of unstable wavelengths. The dam-break wave is unstable for $t \geqslant t_{cr}$ at all wavenumbers within the range (see §3.2)

$$\alpha_\infty(\phi) < \alpha < \infty \quad \text{with} \quad \alpha = \frac{2\pi}{\lambda_0} \frac{V_0^2}{\sin\theta}, \tag{3.62}$$

in which $\alpha_\infty(\phi)$ is given by (3.35). Substituting (3.35) into (3.62), and taking into account (3.54) and (3.55), one has

$$0 < \lambda_0 < \lambda_\infty \equiv \frac{2\pi V_0(X,t)^2}{\alpha_\infty(\phi(X,t))\sin\theta} = \pi \frac{X^{3/2}\sqrt{2X + 9t^2\sin\theta}}{4X + 9t^2\sin\theta}, \quad 0 < X < X_s(t), \quad t_{cr} < t. \tag{3.63}$$

The dependence of λ_∞ with X and t is a relevant result. Firstly, we observe at a fixed location X that λ_∞ decreases as time proceeds, and so we expect the stabilization of small-amplitude unstable disturbances. This fact is corroborated by plotting the velocity U at the gauge station $X = 1500$ in the dam-break numerical simulation already described in §2. Figure 12(*a*) is such a plot starting from $t = 4500$, the instant at which one begins to observe the formation of small-amplitude instability at the free surface. The velocity perturbation has a temporal frequency of 0.1925 (see the power spectral density, denoted by PSD, in figure 12*b*) which remains almost constant until the flow becomes stable ($t = 7000$). The wavelength in the numerical simulation can be estimated from figure 2(*b*) as the ratio between the space domain length to the number of crests to be 10.71, which falls within the range of the theoretical predictions (3.63) with $\lambda_\infty = 65.75$ at $t = 7000$. Taking into account that during the period of time considered in figure 12(*a*) U and its gradient vary, in the location considered, in the ranges 0.15–0.24 and 9.5×10^{-5}–1.5×10^{-4}, respectively, that wavelength corresponds to $0.76 < \alpha < 1.94$, approximately. The ensuing values of ϕ are 0.00128–0.00131. For these values of α, ϕ and $Fr_p = 2.5$, the multiple-scale stability analysis predicts that the
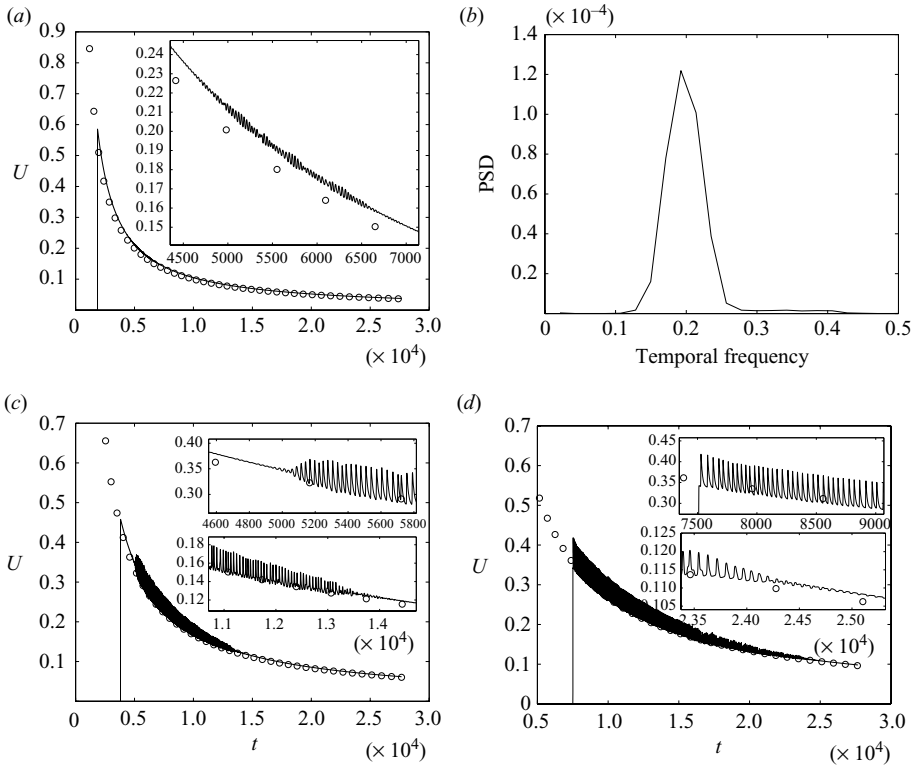
FIGURE 12. Velocity probes at three locations downstream from the gate of the dam: (a) $X = 1500$, (c) $X = 2500$ and (d) $X = 4500$. The numerical solution is plotted in a continuous line and in the circles the asymptotic solution given by (3.54). (b) Power spectral density of the signal (a) after removing the base flow. The numerical simulation corresponds to the same configuration as for figures 2(b) and 2(c).

eigenvalue $\hat{\lambda}_-$ ranges between 0.0157–0.1987i ($t = 4500$) and 0.0058–0.1299i ($t = 7000$). Therefore, the growth rate cannot be too small in order to observe the spontaneous formation of instabilities in the numerical simulation, as in the experiments by Brock (1969), who did not observe the formation of roll waves for Froude numbers below 3.5 for a uniform flow in an inclined channel. On the other hand, the temporal frequency given by the stability analysis agrees quite well with the temporal frequency in the numerical simulation.

Further downstream the amplitude of the instability waves eventually grows to reach the stage at which the velocity signal has the aspect of the classical roll waves (see the inset of figures 12c and 12d). Even nonlinear, large-amplitude hydraulic jumps are attenuated for long times ($t > \{1.4 \times 10^4, 2.5 \times 10^4\}$ at $X = \{2500, 4500\}$, respectively) because of the upstream stabilization of small-amplitude disturbances. Finally, we observe that λ_∞ (3.63) increases as we move downstream, and therefore instability waves may continue developing closer to the flow front, as illustrated in figure 2(c).

4. Summary and conclusions

In this paper, we have considered the stability analysis of the flow after the sudden release of a fixed mass of fluid on an inclined plane formally restricted to relatively long time scales, for which the kinematic regime is valid ($t > t_c$). An asymptotic solution for

long-wave perturbations of small amplitude about kinematic waves with $Fr_p = 2$ has been presented. For larger values of the Froude number, we have accounted for the influence of near-parallel effects on the linear stability criterion by means of a multiple-scale analysis in space and time, and we have found an asymptotic solution for the neutral curve as a function of the plane-parallel Froude number (Fr_p) and a measure of streamwise gradient of the base flow (ϕ). Subsequently, we have designed a numerical experiment, which allows us to compute the nonlinear evolution of small-amplitude perturbations, and so the asymptotic results were checked with those arising from nonlinear numerical simulations, showing a satisfactory agreement between solutions.

We have found that non-uniform time-dependent effects of the background flow stabilize the kinematic wave and raise the critical Froude number required for instability. The well-known stability criterion for plane-parallel flows at high Reynolds number – 'the basic flow is unstable for any wavelength and Froude number larger than 2' (Jeffreys 1925) – differs abruptly from that which results for kinematic waves. These results also differ from that previously reported by Lighthill & Whitham (1955) because of the fundamental role that the non-parallel time-dependent characteristics of the kinematic wave play in the behaviour of small disturbances, which was neglected in their stability analyses. The most noticeable effects are as follows: stabilization of disturbances about basic flows with $Fr_p = 2$; for larger values of the Froude number, the existence of a cutoff wavenumber (α_∞) for the unstable spectrum; and for positive values of ϕ (2.21), the increase of the critical Froude number (Fr_{cr}) required for instability. It is also found that stable waves lengthen as they are convected downstream (see figure 9), and this behaviour also differs from the plane-parallel one, in which waves remain with constant wavelength even when hydraulic jumps are developed. Finally, when applying the asymptotic results to the stability of the dam-break flow (with a tolerance value of $\Phi = 4.25 \times 10^{-3}$) we have established the following conclusions, which are formally valid just for $2 < Fr_p \leqslant Fr_p^* \equiv 2.1626$: dam-break flows over shallow-slope beds, $\theta < 15°$, may first approach the kinematic-wave solution during the period of time $t_c < t < t_{cr}$, subsequently attaining the unstable regime at $t \geqslant t_{cr}$; on steeper bed slopes, $\theta > 15°$, the entire flow field can be unstable at $t < t_c$, and the growth could arise from developments in the time before t_c. The present study predicts the critical time t_{cr} for the onset of roll waves only in the former case. For larger values of the Froude number, $Fr_p^* < Fr_p \ll 5.4641$, though we cannot establish an accurate approximation of t_{cr}, we would expect at a fixed location first the developments of free-surface instabilities, followed by their attenuation until their ultimate extinction (see figure 12), which stabilizes the tail of the dam-break wave, though instability waves may continue developing closer to the flow front, as shown in figure 2(c). The limitations of these results might be caused by neglecting higher-order terms of the base flow (2.8)–(2.9) as well as the non-modal nature of instability waves in the stability analysis. Furthermore, the panorama becomes much more complex in the absence of analytical (or asymptotic) solutions for the frictional dam-break problem on an inclined plane at short and moderate time scales.

We conclude by pointing out the applicability of our stability analysis to more complex rheologies (Ancey 2007), as floods of debris might be approximated by kinematic waves (Arattano & Savage 1994) and usually exhibit the development of surges (Zanuttigh & Lamberti 2007).

Appendix A. Integration of higher-order-terms of the base state

In this paper, the leading-order term in (2.8) and (2.9) was employed to analyse the inception of roll waves in floods on steep inclines. This assumption is likely to be valid under the specific condition $\hat{t} \to \infty$, as discussed in §2. Substituting expansion (2.8)–(2.9) into (2.7), grouping terms $O(\epsilon)$ and using (2.10) and (2.16), one obtains the algebraical relation that follows between H_1 and V_1:

$$H_1 = \frac{1}{8\sin\theta}\left[\frac{4f\hat{x}}{3\hat{t}}V_1 + \frac{4f\hat{x}^3}{81\hat{t}^4\sin\theta}\left(\frac{f}{\tan\theta} - 2\right)\right]. \tag{A 1}$$

Analogously, taking into account (A 1), order ϵ of (2.6) provides for V_1 the equation

$$\frac{\partial V_1}{\partial \hat{t}} + \frac{\hat{x}}{\hat{t}}\frac{\partial V_1}{\partial \hat{x}} + \frac{V_1}{\hat{t}} = \frac{4\hat{x}^2}{81\hat{t}^4\sin\theta}\left(\frac{f}{\tan\theta} - 2\right), \tag{A 2}$$

which can be readily integrated along the family of characteristics

$$\frac{\mathrm{d}\hat{x}}{\mathrm{d}\hat{t}} = \frac{\hat{x}}{\hat{t}}. \tag{A 3}$$

For an arbitrary initial condition $V_1(\hat{x}, \hat{t}=\hat{t}_0) = V_1^0(\hat{x})$, $\hat{t}_0 > 0$, the general solution to (A 2) reads

$$V_1(\hat{x}, \hat{t}) = \frac{\hat{t}_0}{\hat{t}}V_1^0\left(\hat{x}\hat{t}_0/\hat{t}\right) + \left(\frac{f}{\tan\theta} - 2\right)\frac{4\hat{x}^2\log(\hat{t}/\hat{t}_0)}{81\hat{t}^3\sin\theta}. \tag{A 4}$$

The limit $\hat{t} \to \infty$ of (A 1) and (A 4) along the ray $\hat{x}/\hat{t} = \text{constant}$ is zero, and thus it is now evident that both V_1 and H_1 vanish when $\hat{t} \gg \hat{t}_0$.

In general, V_j and H_j $(2 \leqslant j)$ can be determined following the same procedure as for $j=0$ (see §2) and $j=1$ (see above). As a matter of fact, order ϵ^j of (2.7) provides a linear relation between H_j and V_j of type

$$H_j = \frac{fV_0}{4\sin\theta}V_j + \kappa_j\left(V_i, \frac{\partial^k V_i}{\partial \hat{x}^k}, \frac{\partial^k V_i}{\partial \hat{t}^k}; f, \theta\right) \quad \text{with} \quad 0 \leqslant i < j, \quad 0 < j, \quad k \leqslant i. \tag{A 5}$$

It is an easy exercise to show that κ_j-function vanishes along (A 3) as time infinity. Subsequently, (A 5) is substituted into $O(\epsilon^j)$ of (2.6) to yield a linear non-homogeneous hyperbolic first-order partial differential equation, given by

$$\frac{\partial V_j}{\partial \hat{t}} + \frac{3}{2}V_0\frac{\partial V_j}{\partial \hat{x}} + \left(\frac{1}{V_0}\frac{\partial V_0}{\partial \hat{t}} + 3\frac{\partial V_0}{\partial \hat{x}}\right)V_j = \zeta_j\left(V_i, \frac{\partial^k V_i}{\partial \hat{x}^k}, \frac{\partial^k V_i}{\partial \hat{t}^k}; f, \theta\right). \tag{A 6}$$

For $\hat{t} \to \infty$, ζ_j vanishes as κ_j does. Finally, substituting (2.16) into (A 6), and neglecting both κ_j and ζ_j, it follows the general solution

$$V_j(\hat{x}, \hat{t}) = \frac{C_j(\hat{x}/\hat{t})}{\hat{t}}, \quad 1 \leqslant j, \tag{A 7}$$

in which C_j depends on the initial condition. For any C_j, V_j is attenuated as time increases along the ray $\hat{x}/\hat{t} = $ constant. This result is corroborated by the numerical simulation described in §2 (see figure 2), which shows that the leading-order term V_0 (2.16) approaches the numerical solution to the full nonlinear shallow-water equations (2.1) and (2.2) in an increasingly better manner as time proceeds.

Appendix B. Cutoff in wavelength for the spectrum

In §3.3 we have stated that when a disturbance is initially stable (at $\tau = 1$) for $Fr_p > 2$, it remains in the stable region of the stability diagram as time proceeds,

$$\alpha(\xi, \tau) < \alpha_\infty(\phi(\xi, \tau)), \quad 1 \leqslant \tau, \quad 0 \leqslant \xi, \tag{B 1}$$

in which α, ϕ and α_∞ are given by (3.52), (3.53) and (3.35), respectively.

At $\tau = 1$, (B 1) can be written as

$$\mu^2 < q(\phi^o) \equiv \frac{32(1 + \phi^o)^2}{\phi^o(2 + \phi^o)} \quad \text{with} \quad \mu \equiv \frac{\alpha^o}{\phi^o}. \tag{B 2}$$

Notice that when ϕ^o varies from 0 to ∞, $q(\phi^o)$ decreases from ∞ to 32.

Taking into account the definition of α_∞, given by (3.35), and substituting (3.52) and (3.53) into (B 1) yields

$$0 < 32\tilde{\tau}^2 + (32 - \mu^2)(2\tilde{\tau} + 1) \equiv p(\tilde{\tau}, \mu) \quad \text{with} \quad \tilde{\tau} \equiv \frac{\tau}{\phi^o} \geqslant (\phi^o)^{-1} > 0. \tag{B 3}$$

Obviously, $p(\tilde{\tau}, \mu) > 0$ at all $\tilde{\tau}$ when $\mu^2 \leqslant 32$. So (B 1) and (B 2) are readily satisfied, and there is cutoff in wavelength for the spectrum.

Conversely, when $32 < \mu^2$, we find that $p(\tilde{\tau}, \mu) = 0$ for $\tilde{\tau} = \tilde{\tau}_{cr}$,

$$\tilde{\tau}_{cr} \equiv \frac{1}{32}(\mu^2 - 32 + \sqrt{\mu^4 - 32\mu^2}),$$

$p(\tilde{\tau}, \mu) < 0$ for $\tilde{\tau} < \tilde{\tau}_{cr}$ and $0 < p(\tilde{\tau}, \mu)$ for $\tilde{\tau}_{cr} < \tilde{\tau}$. Since a disturbance that is initially stable satisfies the condition $0 < p(1/\phi^o, \mu)$, we conclude that $\tilde{\tau}_{cr} < (\phi^o)^{-1} \leqslant \tilde{\tau}$. This implies that the wave remains in the stable region, and so there is cutoff in wavenumber for the spectrum, as we wanted to prove.

REFERENCES

ANCEY, C. 2007 Plasticity and geophysical flows: a review. *J. Non-Newton. Fluid Mech.* **142**, 4–35.

ANCEY, C., COCHARD, S. & ANDREINI, N. 2009 The dam-break problem for viscous fluids in the high-capillary-number limit. *J. Fluid Mech.* **624**, 1–22.

ANCEY, C., IVERSON, R. M., RENTSCHLER, M. & DENLINGER, R. P. 2008 An exact solution for ideal dam-break floods on steep slopes. *Water Resour. Res.* **44**, W01430.

ARATTANO, M. & SAVAGE, W. Z. 1994 Modelling debris flows as kinematic waves. *Bull. Intl Assoc. Engng Geol.* **49**, 3–13.

BALMFORTH, N. J. & MANDRE, S. 2004 Dynamics of roll waves. *J. Fluid Mech.* **514**, 1–33.

BLAYO, E. & DEBREU, L. 2005 Revisiting open boundary conditions from the point of view of characteristic variables. *Ocean Model.* **9**, 231–252.

BOHORQUEZ, P. 2008 On the wavefront shape and the advancing of the wetting front of a dam-break flood over an inclined plane of arbitrary bottom slope. Roll waves in floods on inclines. In *Numerical Modelling of Hydrodynamics for Water Resources* (ed. P. Garcia-Navarro & E. Playan), pp. 355–366. Taylor and Francis.

BOHORQUEZ, P. & DARBY, S. E. 2008 The use of one- and two-dimensional hydraulic modelling to reconstruct a glacial outburst flood in a steep Alpine valley. *J. Hydrol.* **361**, 240–261.

BOHORQUEZ, P. & FERNANDEZ-FERIA, R. 2008 Transport of suspended sediment under the dam-break flow on an inclined plane bed of arbitrary slope. *Hydrol. Process.* **22** (14), 2615–2633.

BRAUNER, N. & MARON, D. M. 1982 Characteristics of inclined thin films, waviness and the associated mass transfer. *Intl J. Heat Mass Transfer* **25** (1), 99–110.

BROCK, R. R. 1969 Development of roll-wave trains in open channels. *J. Hydraul. Div.* **95**, 1401–1427.

BROOK, B. S., FALLE, S. A. E. G. & PEDLEY, T. J. 1999 Numerical solutions for unsteady gravity-driven flows in collapsible tubes: evolution and roll-wave instability of a steady state. *J. Fluid Mech.* **396**, 223–256.

CASTRO, M., GALLARDO, J. M. & PARÉS, C. 2006 High order finite volume schemes based on reconstruction of states for solving hyperbolic systems with nonconservative products. Applications to shallow-water systems. *Math. Comput.* **75**, 1103–1134.

CASTRO, M., GALLARDO, J. M. & PARÉS, C. 2008 Why many theories of shock waves are necessary: convergence error in formally path-consistent schemes *J. Comput. Phys.* **227**, 8107–8129.

CHANG, H. C., DEMEKHIN, E. A. & KALAIDIN, E. 2000 Coherent structures, self-similarity, and universal roll wave coarsening dynamics. *Phys. Fluids* **12** (9), 2268–2278.

ČRNJARIĆ ŽIC, N., VUKOVIĆ, S. & SOPTA, L. 2004 Balanced finite volume WENO and central WENO schemes for the shallow water and the open-channel flow equations. *J. Comput. Phys.* **200**, 512–548.

DEMEKHIN, E. A., KALAĬDIN, E. N. & SHAPAR', E. M. 2005 On the theory of roll waves in inclined channels. *Dokl. Phys.* **50** (4), 220–222.

DENLINGER, R. P. & O'CONNELL, D. R. H. 2008 Computing nonhydrostatic shallow-water flow over steep terrain. *J. Hydraul. Engng* **134** (11), 1590–1602.

DRESSLER, R. F. 1949 Mathematical solution of the problem of roll-waves in inclined open channels. *Comm. Pure Appl. Math.* **2**, 149–194.

DRESSLER, R. F. 1952 Hydraulic resistance effect upon the dam-break functions. *J. Res. Natl Bur. Stand.* **49**, 217–225.

DRESSLER, R. F. 1954 Comparison of theories and experiments for the hydraulic dam-break wave. In *Assemblée Général de Rome*, vol. 3, pp. 319–328. Intl Assoc. of Hydrology.

DRESSLER, R. F. 1958 Unsteady nonlinear waves in sloping channels. *Proc. R. Soc.* A **247**, 186–198.

DRESSLER, R. F. 1978 New nonlinear shallow-flow equations with curvature. *J. Hydraul. Res.* **16**, 205–222.

DUMBSER, M., ENAUX, C. & TORO, E. F. 2008 Finite volume schemes of very high order accuracy for stiff hyperbolic balance laws. *J. Comput. Phys.* **227**, 3971–4001.

EGUIAZAROFF, I. B. 1935 Regulation of the water level in the reaches of canalized rivers. In *XVI International Congress of Navigation*, Brussels.

FERNANDEZ-FERIA, R. 2006 Dam-break flow for arbitrary slopes of the bottom. *J. Engng Math.* **54** (7), 319–331.

GASTER, M. 1962 A note on the relation between temporally-increasing and spatially-increasing disturbances in hydrodynamic stability. *J. Fluid Mech.* **14**, 222–224.

GOTTLIEB, S., KETCHESON, D. I. & SHU, C.-W. 2009 High order strong stability preserving time discretizations. *J. Sci. Comput.* **38** (3), 251–289.

HOGG, A. J. 2006 Lock-release gravity currents and dam-break flows. *J. Fluid Mech.* **569**, 61–87.

HOGG, A. J. & PRITCHARD, D. 2004 The effects of hydraulic resistance on dam-break and other shallow inertial flows. *J. Fluid Mech.* **501**, 179–212.

HUNT, B. 1982 Asymptotic solution for dam-break problem. *J. Hydraul. Div.* **108** (1), 115–126.

HUNT, B. 1984 Perturbation solution for dam-break floods. *J. Hydraul. Engng* **110** (8), 1058–1071.

HUNT, B. 1987 An inviscid dam-break solution. *J. Hydraul. Res.* **25** (3), 313–327.

HWANG, S. H. & CHANG, H. C. 1987 Turbulent and inertial roll waves in inclined film flow. *Phys. Fluids* **30** (5), 1259–1268.

JÁNOSI, I. M., JAN, D., SZABÓ, K. G. & TÉL, T. 2004 Turbulent drag reduction in dam-break flows. *Exp. Fluids* **37**, 219–229.

JEFFREYS, H. J. 1925 The flow of water in an inclined channel of rectangular section. *Phil. Mag.* **49**, 793–807.

KETCHESON, D. I. & LEVEQUE, R. J. 2008 WENOCLAW: a higher order wave propagation method. In *Hyperbolic Problems: Theory, Numerics, Applications* (ed. S. Benzoni-Gavage & D. Serre), pp. 609–616. Springer.

KLUWICK, A. 2006 The effect of surface topography on weakly nonlinear roll waves. *Proc. Appl. Math. Mech.* **6**, 607–608.

LAUBER, G. & HAGER, W. H. 1998*a* Experiments to dambreak wave: horizontal channel. *J. Hydraul. Res.* **36** (3), 291–307.

LAUBER, G. & HAGER, W. H. 1998*b* Experiments to dambreak wave: sloping channel. *J. Hydraul. Res.* **36** (5), 761–773.

LIGHTHILL, M. J. & WHITHAM, G. B. 1955 On kinematic waves. Part I. Flood movement in long rivers. Part II. Theory of traffic flow on long crowded roads. *Proc. R. Soc.* A **229**, 281–345.

LOGAN, M. & IVERSON, R. M. 2007 Video documentation of experiments at the USGS debris-flow flume 1992–2006. *Tech Rep.* Open-File Report 2007-1315. US Geological Survey. http://pubs.usgs.gov/of/2007/1315/.

MARTIN, J. C. & MOYCE, W. J. 1952 Part IV. An experimental study of the collapse of liquid columns on a rigid horizontal plane. *Phil. Trans. R. Soc.* A **224** (88), 312–324.

NEEDHAM, D. J. & MERKIN, J. H. 1984 On roll waves down an open inclined channel. *Proc. R. Soc.* A **394** (1807), 259–278.

NOELLE, S., XING, Y. & SHU, C.-W. 2007 High-order well-balanced finite volume WENO schemes for shallow water equation with moving water. *J. Comput. Phys.* **226**, 29–58.

PRITCHARD, D. 2005 On fine sediment transport by a flood surge. *J. Fluid Mech.* **543**, 239–248.

PROKOPIOU, TH., CHENG, M. & CHANG, H. C. 1991 Long waves on inclined films at high Reynolds number. *J. Fluid Mech.* **222**, 665–691.

RITTER, A. 1892 Die fortpflanzung der wasserwellen. *Z. Verein. Deutch. Ing.* **36**, 947–954.

RUYER-QUIL, C. 2006 Hydrodynamic instability of a film flowing down an inclined plane: modelling, mechanisms and analogy to river flows. In *Wave Dynamics and Stability of Thin Film Flow Systems* (ed. R. Usha, A. Sharma & B. S. Dandapat), pp. 106–169. Narosa.

DE SAINT-VENANT, A. J. C. 1871 Théorie du mouvement non-permanent des eaux, avec application aux crues des riviìere at à l'introduction des marées dans leur lit. *C. R. Acad. Sci. Paris* **73**, 147–154.

SCHMID, P. J. 2007 Nonmodal stability theory. *Annu. Rev. Fluid Mech.* **39**, 129–162.

SCHMID, P. J. & HENNINGSON, D. S. 2001 *Stability and Transition in Shear Flows*. Springer.

SCHOKLISTSCH, A 1917 über dambruchwellen. *Sitzber Akad. Wiss. Wien.* **126**, 1489–1514.

SHU, C.-W. 2009 High order weighted essentially nonoscillatory schemes for convection dominated problems. *SIAM Rev.* **51**, 82–126.

WEIR, G. J 1983 The asymptotic behaviour of simple kinematic waves of finite volume. *Proc. R. Soc.* A **387**, 459–467.

WHITHAM, G. B. 1955 The effects of hydraulic resistance in the dam-break problem. *Proc. R. Soc.* A **227**, 399–407.

WHITHAM, G. B. 1974 *Linear and Nonlinear Waves*. Wiley.

XING, Y. & SHU, C.-W. 2005 High order finite difference WENO schemes with the exact conservation property for the shallow water equations. *J. Comput. Phys.* **208**, 206–227.

YU, J. & KEVORKIAN, J. 1992 Nonlinear evolution of small disturbances into roll waves in an inclined open channel. *J. Fluid Mech.* **243**, 575–594.

ZANUTTIGH, B. & LAMBERTI, A. 2007 Instability and surge development in debris flow. *Rev. Geophys.* **45**, RG3006.